REPORT DOCUMENTATION PAGE

Form Approved
OMB NO. 0704-0188

1. AGENCY USE ONLY (Leave Blank)	2. REPORT DATE 3/14/02	3. REPORT TYPE AND DATES COVERED Final 9/01/01-12/19/01 12-20-99 — 12-19-01

4. TITLE AND SUBTITLE

A Multi-Parameter Snow Sounding Probe

5. FUNDING NUMBERS

C. DAAD19-00-C-0010

6. AUTHOR(S)

Robert L Foster

7. PERFORMING ORGANIZATION NAME(S) AND ADDRESS(ES)

Capacitec Inc
PO Box 819   Ayer MA   01432-0819

8. PERFORMING ORGANIZATION REPORT NUMBER   8

9. SPONSORING / MONITORING AGENCY NAME(S) AND ADDRESS(ES)

U. S. Army Research Office
P.O. Box 12211
Research Triangle Park, NC 27709-2211

10. SPONSORING / MONITORING AGENCY REPORT NUMBER

40336-EV-SB2

40336.1 - EV-SB2

11. SUPPLEMENTARY NOTES

The views, opinions and/or findings contained in this report are those of the author(s) and should not be construed as an official Department of the Army position, policy or decision, unless so designated by other documentation.

12 a. DISTRIBUTION / AVAILABILITY STATEMENT

Approved for public release; distribution unlimited.

12 b. DISTRIBUTION CODE

13. ABSTRACT (Maximum 200 words)

REPORT DEVELOPED UNDER SBIR CONTRACT

Vertical soundings of the snowpack are essential diagnostic tools for snow hydrologists and avalanche forecasters. Hydrologists require quantitative profiles of snow density from which they can infer the total amount of snow coverage in a region. Because variations in altitude and terrain can result in widely different coverage, they must dig a relatively large number of pits or extract and weigh many core samples to estimate the snow water equivalent from the corresponding average density. Avalanche forecasters are concerned with recent precipitation and relatively rapid metamorphosis of buried snow layers. While they too require a large number of pits to assess the avalanche potential of a basin, they often perform a more qualitative inspection aimed at identifying the presence and depth of weak layers in a relatively immature snowpack. To address these needs, we have developed a penetration field-portable capacitance probe capable of recording profiles of complex dielectric permittivity and temperature through the snowpack. Density profiles were acquired without the need for multiple excavations. The probe consists of a lance with a wedged capacitance tip allowing penetration to variable depths. The tip is connected to a portable signal conditioner for data processing and storage.

14. SUBJECT TERMS

SBIR Report

20030227 115

15. NUMBER OF PAGES 61
16. PRICE CODE

17. SECURITY CLASSIFICATION OR REPORT UNCLASSIFIED	18. SECURITY CLASSIFICATION ON THIS PAGE UNCLASSIFIED	19. SECURITY CLASSIFICATION OF ABSTRACT UNCLASSIFIED	20. LIMITATION OF ABSTRACT UL

NSN 7540-01-280-5500

Standard Form 298 (Rev.2-89)
Prescribed by ANSI Std. 239-18
298-102

▦ Capacitec

AYER, MA

DAAD19-00-C-0010

FINAL REPORT

A MULTI-PARAMETER SNOW

SOUNDING PROBE

A Multi-Parameter Snow Sounding Probe

Capacitec, Inc

Final report to the US Army Research Office

Michel Y. Louge

Cornell University
Sibley School of Mechanical and Aerospace Engineering
192 Rhodes Hall
Ithaca, NY 14853

Robert L. Foster, Kelly Clifford and Bryan Manning

Capacitec, Inc.
PO Box 819
Ayer, MA 01432-0819

Contract DAAD19-00-C-0010

EXECUTIVE SUMMARY

Vertical soundings of the snowpack are essential diagnostic tools for snow hydrologists and avalanche forecasters. Hydrologists require quantitative profiles of snow density from which they can infer the total amount of snow coverage in a region. Because variations in altitude and terrain can result in widely different coverage, they must dig a relatively large number of pits or extract and weigh many core samples to estimate the snow water equivalent from the corresponding average density.

Avalanche forecasters are concerned with recent precipitation and relatively rapid metamorphosis of buried snow layers. While they too require a large number of pits to assess the avalanche potential of a basin, they often perform a more qualitative inspection aimed at identifying the presence and depth of weak layers in a relatively immature snowpack.

To address these needs, we have developed a penetration field-portable capacitance probe capable of recording profiles of complex dielectric permittivity and temperature through the snowpack. Our vision is to acquire density profiles without the need for multiple excavations. The probe consists of a lance with a wedged capacitance tip allowing penetration to variable depths. The tip is connected to a portable signal conditioner for data processing and storage.

We established feasibility of this concept in Phase I of the SBIR grant. An important objective of Phase II was to develop an instrument responding to the needs of the

snow community. To that end, we have conducted a survey of snow professionals in an effort to define the characteristics of the commercial instrument and determine the level of sophistication and cost that potential customers will expect.

Another objective of Phase II was to find a frequency of the probe carrier signal that would maintain stability of the amplifier for a wide variety of snows, while keeping the signal sensitive to small changes in the density and morphology of snow layers. Accordingly, we tested three devices operating, respectively, at 2.25, 3.9 and 15.6 kHz.

Probes operating at those respective frequencies were tested near Salt Lake City in cooperation with the University of Utah and the Utah Department of Transportation. There, we recorded the real and imaginary parts of the snow dielectric constant through typical winter snowpacks. The amplifier operating at 2.25 kHz exhibited the greatest stability, even with snows of considerable wetness. However, because its output was not linearly related to the probe impedance, its measurements of dielectric constant were only qualitative. In contrast, the amplifiers at 3.9 kHz and 15.6 KHz generated a linear output signal. However, the amplifier at 15.6 kHz was only stable for dry snows. Thus, the final amplifier was designed with a carrier frequency of 3.9 kHz, which offered the best compromise between stability and linearity. We also added to this instrument a thermistor to record temperature depth profiles.

Using independent calibrations, measurements of the dielectric modulus at 3.9 kHz and 15.6 kHz provided an accurate profile of snow density and revealed the presence of layers that were later confirmed by the excavation of detailed snow cover profiles. In particular, we found that, for samples originating from the same basin and exhibiting similar temperatures, the real part of the dielectric constant was well correlated with snow density through a single empirical fit, despite wide variations in snow morphology or the presence of impurities.

We evaluated two different probe tips in the field trials. Although the corresponding signals did not reveal any obvious difference between them, we retained the smallest and least invasive of the two for further commercial development.

We designed a user-friendly interface for this instrument based upon a Palm Pilot data acquisition system. For convenience, we employed an opto-mechanical method to record the depth at which permittivity and temperature were recorded.

Because snows exhibit different complex dielectric constants in different basins, we also designed a calibration instrument, the "snow press," to record the dependence of this

parameter on density. Our expectation is that customers will conduct calibrations once every season and use the results to interpret data from the capacitance sounding probe.

Finally, we explored the possibility of exploiting small, inexpensive infrared sensors to provide an independent measurement of grain size. To that end, after characterizing their directional emissivity, we simulated their optical behavior in a pack of transparent glass beads using a Monte-Carlo algorithm, and recorded their actual response to beads of known sizes in the laboratory. The experiments and simulations revealed that this inexpensive instrument can distinguish grain sizes as large as 1 mm. This promising result suggests that this optical instrument should be further developed. In particular, our simulations have pointed to a simple re-design of the chip that would distinguish grains of size up to 3 mm.

1. INTRODUCTION

In a workshop organized by the US Army Research Office in October 1995, the snow science community assigned its highest priority to the development of a multi-parameter snow penetration probe capable of recording physical parameters governing mechanical properties of the snow pack (Brown and Dent, 1996).

The recommendation was inspired by the report of Dr. Hansueli Gubler, a leading instrumentation scientist, and by our recent application of capacitance techniques to the measurement of snow density and velocity (Louge, et al, 1997). We began Phase II of this SBIR grant by conducting a survey of snow professionals. The results, which are summarized in an Appendix, highlighted the needs of the snow community. Among the desired parameters (density, temperature, grain size, wetness and cohesion), the suggestion was to begin with a capacitance measurement of dielectric permittivity to infer local density, temperature and depth.

To address these needs, we have developed a penetration field-portable capacitance probe capable of recording profiles of dielectric permittivity through the snowpack. Our vision is to acquire density profiles without the need for multiple excavations. The probe consists of a lance with a wedged capacitance tip allowing penetration to variable depths. The tip is connected to a portable signal conditioner for data processing and storage. The instrument also records temperature and its evaluates depth automatically.

This report describes the new instrument and summarizes its tests in typical snow packs. We begin with a short background on the principle of our capacitance measurements. We then describe various incarnations of the instrument and the

3

corresponding tests. Finally, we report our preliminary development of an optical sensor for measuring grain size, which may complement our instrument in the future.

2. BACKGROUND ON CAPACITANCE MEASUREMENTS

The purpose of our capacitance instrumentation is to record accurately the complex dielectric permittivity of snow in a well-defined measurement volume. Because the detailed design of our electronics is a proprietary trade secret, we provide here an equivalent circuit that closely represents the actual behavior of our instruments with typical snows.

As Fig. 1 illustrates, generic probes feature three conductors called the "sensor", "ground" and "guard" electrodes. The electronics records the impedance Z between sensor and ground, while a buffer amplifier maintains the guard at precisely the same sinusoidal voltage as the sensor's. Because it absorbs distortions of the electric field caused by external interferences, the guard protects the sensor from stray capacitances. In addition, because the sensor is connected to the processing circuits using a guarded coaxial cable, the cable capacitance does not participate in the measurement. By eliminating stray and cable capacitances, our technique can detect capacitances three to six orders of magnitude smaller than conventional bridges of similar cost.

To ensure proper operation of the guard electrode, the electronics must maintain the guard voltage v_g equal to the sensor voltage v_s. This is accomplished by sampling v_s through a buffer amplifier of unity gain. This buffer has a suitably high input impedance to avoid disturbing the sensor circuit. Further protection of the sensor circuit from external interferences is accomplished by surrounding it with a guarded shield. The output of the system is the rectified guard voltage V, which the buffer keeps proportional to the amplitude of the sensor voltage.

Another objective of the electronics is to pass a sinusoidal current of constant amplitude through the test impedance Z. To this end, the carrier oscillator generates a voltage v_r of constant, albeit user-adjustable, amplitude. The amplitude of the sensor current i is kept constant by controlling the voltage $(v_s - v_1)$ across the reference impedance Z_r. This is achieved by sampling the sensor voltage v_s through the buffer, adding or subtracting the difference $(v_s - v_1)$ to the oscillator voltage, and feeding the result to the reference impedance through an amplifier of high gain H (Fig. 1).
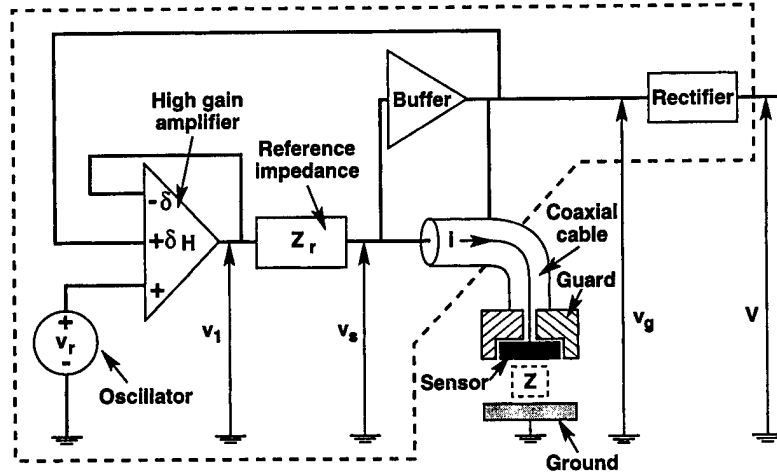
4

Fig. 1. Schematic of the electronic system. The dashed lines represent the physical boundary of the processing circuits. Z is the impedance between sensor and ground.

Assuming negligible current input into the amplifiers, the voltage v_1 into the reference impedance is

$$v_1 = H (v_r + \delta v_g - \delta v_1) = i (Z_r + Z) , \tag{1}$$

while the guard voltage is

$$v_g = v_s = Z i. \tag{2}$$

Eliminating v_1 from Eqs. (1) and (2) yields

$$\frac{v_r}{v_g} = \frac{1}{H} + \frac{Z_r}{Z} \left(\frac{1+\delta H}{H}\right) \tag{3}$$

and

$$i = \frac{v_r}{Z_r} \left(\frac{1}{\left(\frac{Z}{Z_r}\right)\left(\frac{1}{H}\right) + \left(\frac{1+\delta H}{H}\right)}\right) . \tag{4}$$

Because H is assumed to be large and real, inspection of Eq. (4) indicates that the current is nearly independent of Z,

$$i \approx \delta v_r/Z_r , \tag{5}$$

and the modulus of Eq. (3) is, to a good approximation,

$$\frac{|v_r|}{|v_g|} \approx \frac{|Z_r|}{|Z|} . \tag{6}$$

5

Because rectification produces a voltage proportional to v_g, the output V is itself proportional to the modulus of Z.

For powders with negligible imaginary part of the permittivity, $Z = 1/j2\pi fC$, where f is the frequency of the oscillator and $j^2 = -1$. In this case, the system produces a rectified output voltage that is related to C, the capacitance between the ground and sensor surfaces, through the empirical relation

$$V = Q_s/gC, \tag{7}$$

where Q_s is a system constant and g is an adjustable parameter. From Eq. (7), the effective dielectric constant ε_e of a homogeneous suspension covering the probe is obtained by forming the ratio of V_0, the rectified probe output in air, and V, the output in the presence of the dielectric powder of interest,

$$\varepsilon_e \equiv C/C_0 = V_0/V, \tag{8}$$

where C_0 is the probe capacitance in air. For a dielectric powder, it remains to infer the volume fraction from the measurement of ε_e. This is achieved by analyzing or calibrating the dielectric behavior of the suspension (Louge and Opie, 1990).

Unlike dielectric powders like glass or plastic beads, snow possesses a significant imaginary part of the permittivity. In this case, the voltage ratio V_0/V yields the modulus of Z,

$$\frac{V_0}{V} = \left| \frac{Z_0}{Z} \right| = \frac{1}{2\pi f\, C_0\, |Z|}\,, \tag{9}$$

where Z_0 is the probe's impedance in air. For isotropic media, the electric displacement D and the electric intensity E are colinear vectors; however, because they are not generally in phase, the effective dielectric constant of snow ε_e may exhibit real and imaginary parts,

$$\varepsilon_e \equiv D/\sigma_0\, E = \varepsilon' - j\, \varepsilon''\,, \tag{10}$$

where ε' and ε'' are both functions of frequency and $\sigma_0 = 8.854\ 10^{-12}$ F/m is the dielectric permittivity of free space and, to a good approximation, of air. The corresponding impedance between sensor and ground is

$$Z = \frac{1}{\ell\, 2\pi f\, \sigma_0\, (\varepsilon'' + j\varepsilon')}\,. \tag{11}$$

In this expression, ℓ is a characteristic length of the capacitance probe geometry,

$$\ell \equiv C_0/\sigma_0\,. \tag{12}$$

In the presence of a homogeneous, isotropic suspension, ℓ is independent of ε_e. Thus, from Eqs. (9) through (12), the voltage ratio yields the modulus of ε_e,

$$\frac{V_0}{V} = \sqrt{\varepsilon''^2 + \varepsilon'^2} . \tag{13}$$

In order to resolve both components of ε_e, we exploit the phase lag ϕ between v_r and v_g, which are both readily available for measurement. From Eq. (3),

$$\tan \phi = \frac{1 - \frac{m}{n} \frac{\varepsilon'}{\varepsilon''}}{\frac{\varepsilon'}{\varepsilon''} + \frac{m}{n} + \frac{1}{2\pi f \, \sigma_0 \, \varepsilon'' \, \ell \, n(1+\delta H)}} . \tag{14}$$

where m and n are the real and imaginary parts of the conjugate of Z_r,

$$Z_r \equiv m - n j . \tag{15}$$

For the amplifier operating at 15.6 kHz, Z_r is purely capacitive, so m = 0. Note that, in order to permit successful measurements of capacitance in air, the condition

$$|2\pi f \, \sigma_0 \, \ell \, n(1+\delta H)| \gg 1 \tag{16}$$

must be satisfied to let Eq. (6) be a valid approximation of Eq. (3). Consequently, for the 15.6 kHz amplifier, Eq. (14) reduces to

$$|\tan \phi| \approx \frac{\varepsilon''}{\varepsilon'} , \tag{17}$$

so the phase lag between v_r and v_g is a direct measure of the "loss tangent" ($\varepsilon''/\varepsilon'$).
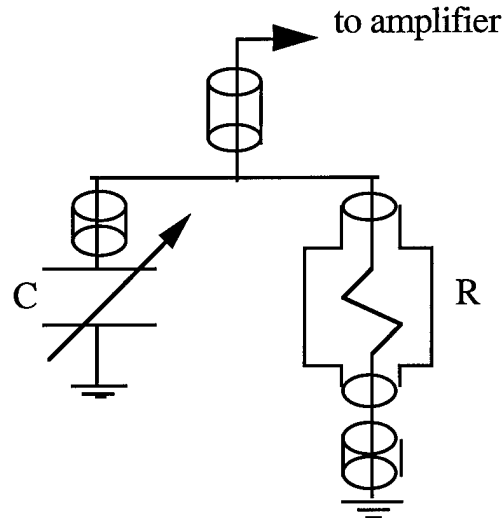

Fig. 2. Circuit for testing the characteristics of the amplifier at 3.9 kHz.

For the amplifier at 3.9 kHz, the determination of ε' and ε'' requires a more complicated solution involving Eqs. (13) and (14). In turn, this solution requires knowing the constants m(1+δH) and n(1+δH), as well as the characteristic length ℓ for each probe. To measure the two constants, we connected the 3.9 kHz amplifier to the circuit of Fig. 2 and we recorded the resulting phase and output voltage (Appendix 1). We found m(1+δH) = 20 MΩ and n(1+δH) = 416 MΩ. We then inferred the dielectric properties of snow soundings using the procedure outlined in Appendix 2.

3. DIELECTRIC PROPERTIES OF SNOW

While this technique produces accurate records of the dielectric permittivity, its principal challenge is to relate local measurements of ε_e to other snow properties such as density and morphology. To do so, we evaluated the dielectric constant of various samples in the capacitance "snow press" of Louge, et al (1997). This instrument includes a grounded piston traveling in a plastic cylinder of 102 mm diameter (Fig. 3). The base features a circular sensor surface of 25 mm diameter surrounded by a guard plate of 197 mm diameter. Gaps in the range 12 to 76 mm between piston and base are recorded using a depth micrometer. (The micrometer is in fact unnecessary. Its function may be served by merely counting the number of complete rotations of the screw that lowers the piston). Because these gaps are smaller than the lateral width of the guard surface, the electric field lines shed by the sensor are straight and parallel to the axis of the cylinder. After a sample is introduced in the press, the piston is progressively lowered to bring snow to denser compactions while the corresponding values of ε_e are measured.
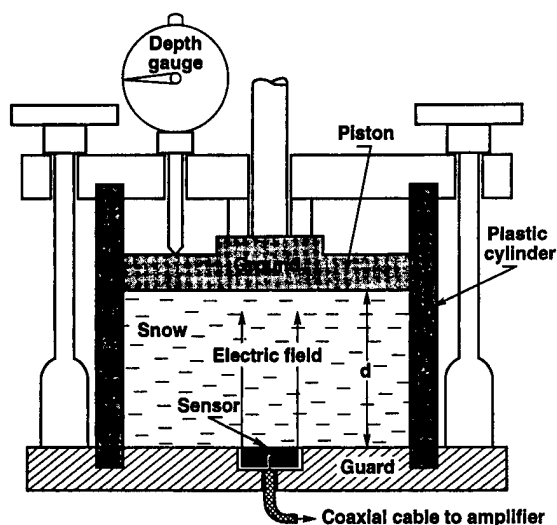

Fig. 3. The "snow press" of Louge, et al (1997).

Before a series of calibration tests, the amplitude of the oscillator is adjusted to ensure that the guard voltage is a pure sine wave without noticeable distortion at a gap $d_0 \approx 51$ mm. At this gap, the amplifier produces an output voltage V_0 in the absence of snow. After removing the piston assembly, snow is gently introduced in the press to nearly the same depth. The piston is then slowly brought to touch the upper surface of the sample. It is progressively lowered to bring snow to denser compactions. At each new position of the piston, snow is allowed to equilibrate volumetrically for a few seconds before the output V, phase ϕ between oscillator and guard and depth d are recorded. Because the press capacitance in air is inversely proportional to depth, the modulus of the dielectric constant is

$$|\varepsilon_e| = \sqrt{\varepsilon'^2 + \varepsilon''^2} = \frac{d}{d_0} \frac{V_0}{V} , \tag{18}$$

while the phase yields the magnitudes of ε' and ε'', as outlined earlier. After the test, the sample is extracted and weighed in order to calculate its overall density at each position. Assuming homogeneous snow distribution in the press, the average density of the compressed sample is

$$\rho = M/d\, A_p , \tag{19}$$

where M is the sample mass and A_p is the cross-sectional area of the piston.

We also developed a portable version of the snow press in Phase II (Fig. 4). Its bore diameter of 38.2 mm was designed to match the federal core sampler. However, the relatively small mass of the corresponding snow sample made the resulting calibration too uncertain, unless the user saves the snow sample in hermetic "Ziploc" bags for later weighing. Thus, for commercial purposes, we have decided to manufacture and sell a larger snow press of dimensions similar to those of Louge, et al (1997).
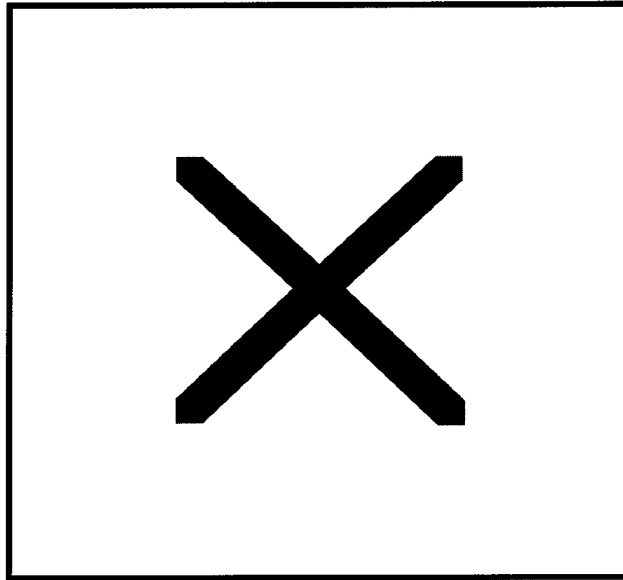
Fig. 4. Portable snow press.

We carried out a series of tests with the Utah Department of Transportation and the University of Utah at the mountain resort of Alta near Salt Lake City in the winters of 1997, 2000 and 2001. For the amplifiers operated at 15.6 kHz and 3.9 kHz, we found that the real part of ε_e correlates well with snow density, thus producing an empirical calibration valid for any type of snow present in the pack. Louge, et al (1997,1998) did not identify this correlation. Instead, they related the modulus $|\varepsilon_e|$ of the dielectric constant with density. Our observations indicate that, while $|\varepsilon_e|$ may be reasonably well correlated with density at 15.6 kHz, the correlation is less compelling at 3.9 kHz. In fact, overall, relating density with ε' appears to be more accurate. Tables 1 and 2 briefly describes the snows tested at the two frequencies. Figures 5 and 6 illustrates the corresponding correlations between ρ and ε'. Figure 7 indicates that ε' is larger at 3.9 kHz than at 15.6 kHz. Thus, the signal-to-noise ratio is stronger at 3.9 kHz. As the next section will show, these empirical relations can then be used to extract accurate density profiles through the snow pack.

Table 1 - Snow calibrations with the 15.6 kHz amplifier

sample	T_{press} °C	T_{pack} °C	description	loss tangent without compression
3/1/97-1			mixed 75% rounds + facets 0.5mm	0.42
3/1/97-2	-2.4		mixed 75% rounds + facets 0.5mm	0.36
3/1/97-3	-3°	-8.2	decomposing stellar & dendrites	0.32

10

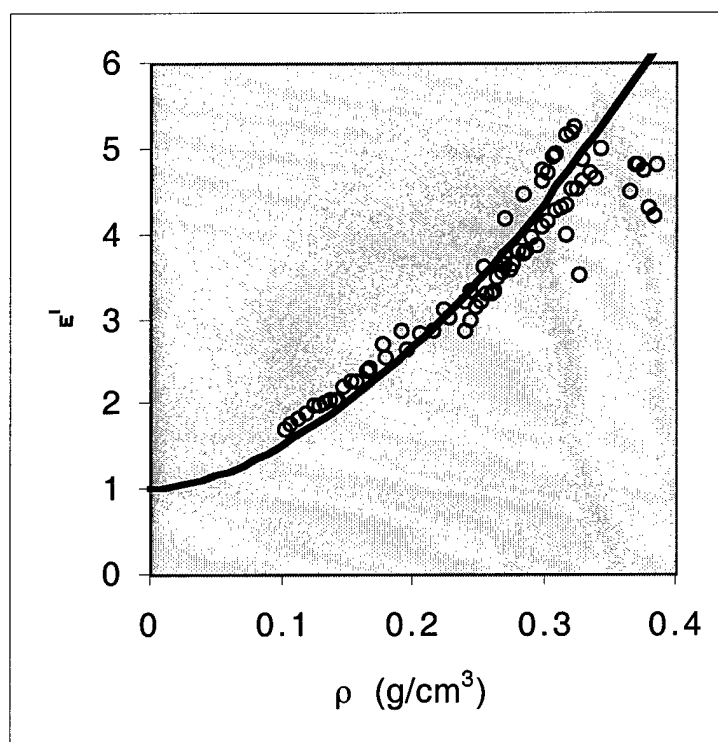| 3/1/97-4 | -3° | -8.2 | decomposing stellar & dendrites | 0.32 |
3/1/97-5			mixed facets decomposing to round, 2mm below melt freeze layer	0.38
3/1/97-6	-2.9	-5.4	0.5mm rounds + 1mm facets (30% of total)	0.42
3/1/97-7	-4.5°	-5.3°	0.5mm rounds + 1mm facets (25% of total)	0.42

Fig. 5. Real part of the snow dielectric constant versus density recorded in the snow press for the amplifier at 15.6 kHz. The solid line is a least-squares fit through the data of the form $\varepsilon' = 1+(\rho/\rho_0)^{1.7}$ with $\rho_0 \approx 0.149$ g/cm^3.
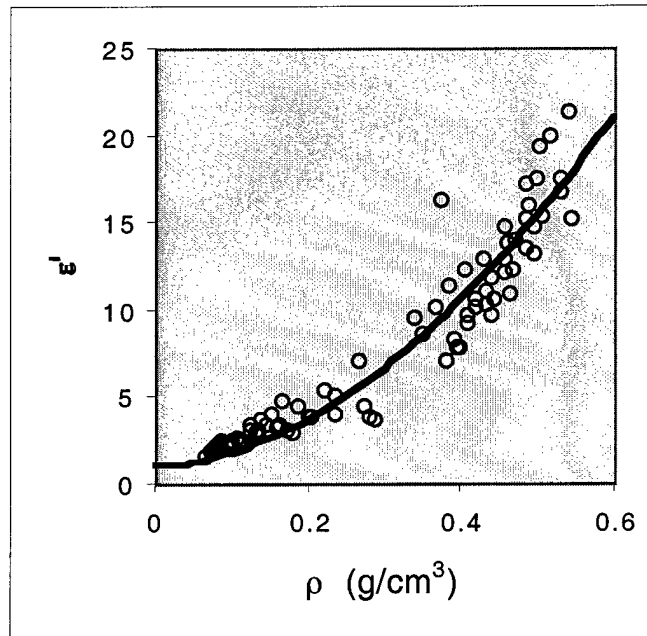
Fig. 6. Real part of the snow dielectric constant versus density recorded in the snow press for the amplifier at 3.9 kHz. The solid line is a least-squares fit through the data of the form

$$\varepsilon' = 1+(\rho/\rho_0)^{1.8} \text{ with } \rho_0 \approx 0.116 \text{ g/cm}^3.$$

Table 2 - Snow calibrations with the 3.9 kHz amplifier

sample	T_{press} °C	T_{pack} °C	description	loss tangent without compression
2/23 - 5	-2.7	-1.8	fresh snow	1.10
2/23 - 9	-2.4		fresh snow	1.05
2/23 - 6	-2.8	-2.8	still angles going to rounds, medium snow	0.96
2/23 - 10	-3.1	-2.8	still angles going to rounds, medium snow	0.81
2/23 - 7	1.4	2.6	faceted old 1mm	0.52
2/23 - 11	-3.1	-1.9	faceted old 1mm	0.60
2/23 - 8	-1.4	-1.9	melt-freeze crust	0.64
2/25 - 1	-3.1	-3.6	partially decomposed new snow, 1.5mm, 100 kg/m³	0.28
2/25 -2		-2.4	well-bonded 0.25-0.50mm small rounds, mid-way pack, 300 kg/m³	1.06
2/25 -3		-1.6	slowly stabilizing depth hoar, angular, coarse, polygrain, moist 1mm, wet depth	0.58
2/25 -4		-1.4	surface snow, stellar dendrites, 20% 1.5mm graupel	0.82
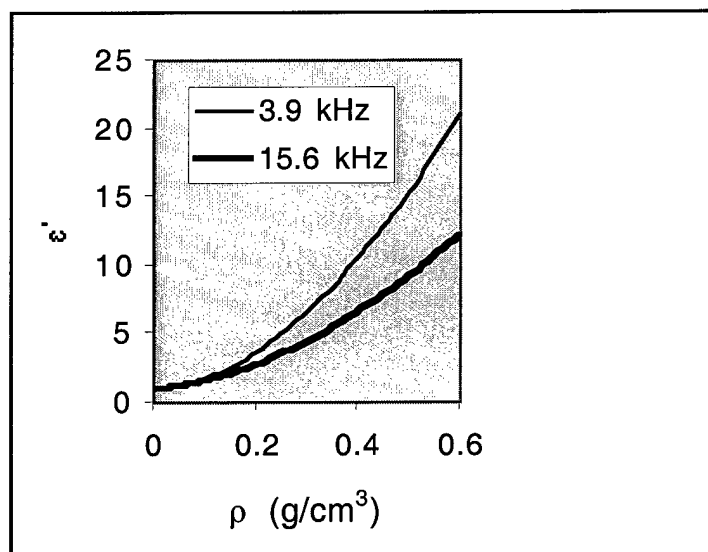
Fig. 7. Growth of the real part of the dielectric constant with snow density at 3.9 kHz (thin line) and 15.6 kHz (thick line) according to the least-squares fits of Figs. 5 and 6.

The calibrations also revealed that the imaginary part of the dielectric constant is a promising way to identify the signature of specific layers in the snow pack. As Table 2 indicates, the loss tangent $\varepsilon''/\varepsilon'$ of different uncompacted snows spans a wide range at 3.9 kHz. Figure 8 shows similar information against snow density. However, the data at 15.6 kHz reveal less dramatic variations of this ratio among the different kinds of snows available in the pack. This observation, together with the stronger real parts exhibited by snow response at 3.9 kHz (Fig. 7), indicates that the amplifier at 3.9 kHz is a better choice for field measurements.

However, as it stands now, we have not yet been able to correlate the imaginary part of the dielectric constant with another intrinsic property of snow. While our observations clearly indicate that the real part is chiefly a function of snow density, we can only state that the imaginary part exhibits wide variations among snow types that may serve to identify their signature in the pack. Our conjecture is that the imaginary part also rises with the presence of ice and/or liquid water. Further field tests are needed to confirm this conjecture. We will later return to this point when discussing the field tests of snow stratigraphy. First, we describe the snow probe.
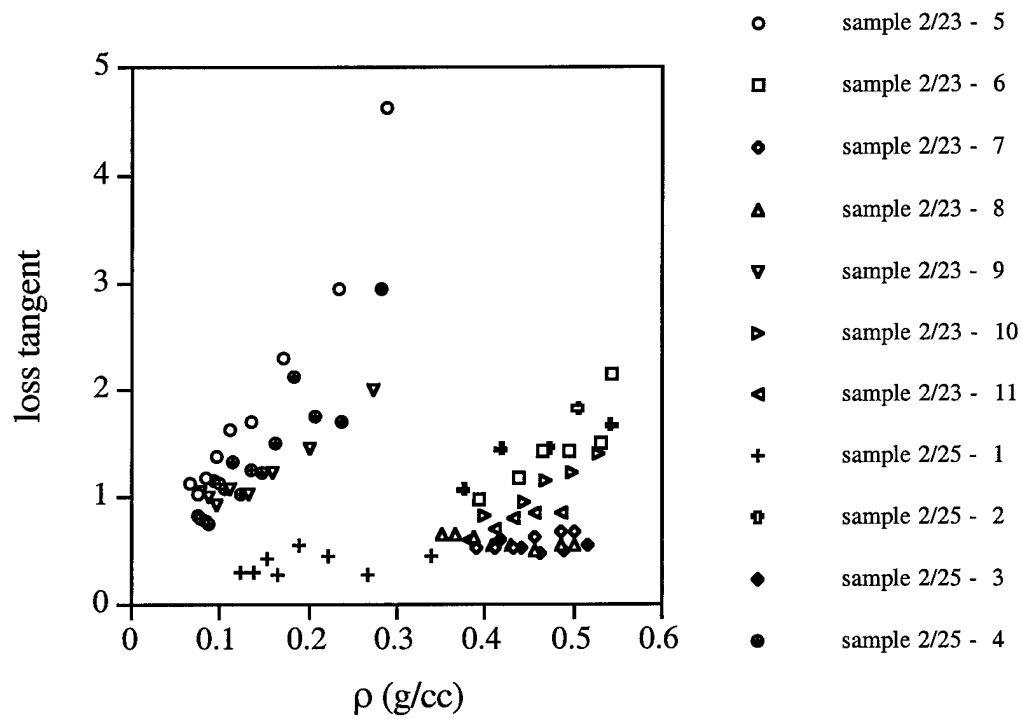
Fig. 8. Loss tangent ε"/ε' versus snow density for the samples shown in Table 2.

4. SNOW SOUNDING PROBE

In this technique, we follow others (eg, Kuroiwa, 1967; Denoth, et al, 1984) in assuming that the snow sample contained in the probe's measurement volume is sufficiently isotropic and homogeneous to possess an effective dielectric constant satisfying Eq. (10).

In Phase I, we designed, manufactured and tested a first prototype of the sounding probe. Its tip, which is mounted at the end of a rigid lance, was cut at an angle of 10° to allow penetration through the pack without disturbing snow density near its frontal surface. The flat sensor/guard assembly is sketched in Fig. 9. The sensor consists of two rectangular conductive surfaces located on either side of the vertical symmetry axis and surrounded by a relatively tall guard. The periphery of the tip is held at the reference voltage.
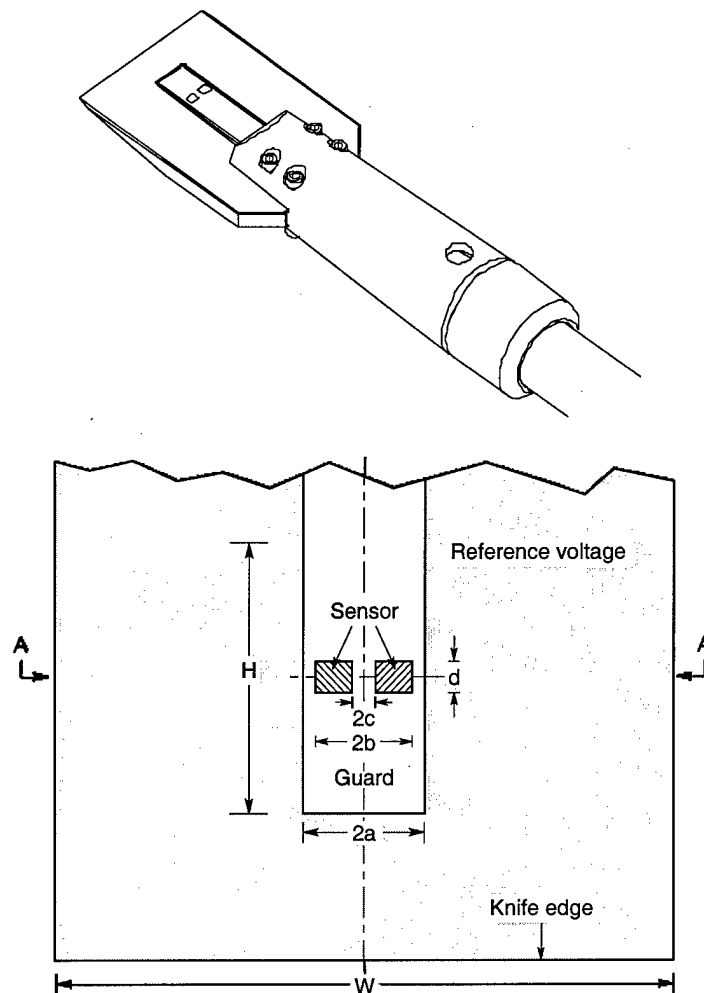
Fig. 9. Tip of the penetration probe. (a) Perspective and (b) front view.

To achieve a finite measurement volume in this geometry, we followed Louge (1995) and located the guard surface on the axis. In a homogeneous medium, this placement lets the sensors shed horizontal, circular electric field lines bounding a measurement volume of thickness equal to the sensors' height.

Figure 10 is a sketch of the quasi-two dimensional electric field emanating from the sensors. Because the frequency of the oscillator is small, the field equation has negligible unsteady terms. It further reduces to the Laplace equation in the absence of free charges in the suspension. Because the Laplace equation is linear, the identical excitation of guard and sensor may be treated as a voltage of fixed amplitude $\tilde{V}$ over the entire guard/sensor assembly. In this case, voltage singularities are located at the boundary between the ground and the guard/sensor assembly (Fig. 10).
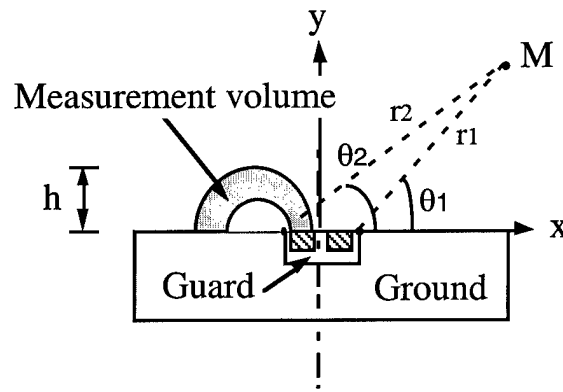
Fig. 10. Section AA showing measurement volume and notation. In this two-dimensional configuration, the section can be represented as the complex plane. Voltage singularities are located between guard and ground.

For this symmetric configuration, it is instructive to derive the electric field near the probe from two-dimensional complex solutions of the Laplace equation. For simplicity, we consider a two-dimensional homogeneous medium above two adjacent equipotential surfaces held at different voltages. The first surface represents the guard/sensor assembly. The second surface is the ground. In this analysis, we ignore the thin dielectric layer that insulates the three electrodes from one another. The complex function that satisfies the conditions $v = \tilde{V}$ for $x \in]-a,+a[$ and $v = 0$ elsewhere is

$$\Phi = \frac{\tilde{V}}{\pi} \left([\theta_1-\theta_2] + j \ln(\frac{r_2}{r_1}) \right), \tag{20}$$

where the angles and radii are shown in Fig. 10. The corresponding voltage distribution is

$$v = (\tilde{V}/\pi)(\theta_1 - \theta_2). \tag{21}$$

16

On an electric field line, the imaginary part of Φ and, consequently, the ratio r_2/r_1, are constant. The field lines are therefore a family of circles of radius R with center located on the axis at an abscissa x_c satisfying

$$(R/a)^2 + (x_c/a)^2 = 1 , \qquad (22)$$

where a and other dimensional symbols are shown in Fig. 9b. The electric field arising from the complex potential Φ is

$$\mathbf{E} = -\nabla v , \qquad (23)$$

and the magnitude of $\mathbf{E}$ at the wall determines the charge distribution there,

$$\mathbf{E} = (\xi / \sigma_0) \, \mathbf{n} , \qquad (24)$$

where ξ is the charge surface density and $\mathbf{n}$ is the outward normal to the plane. Combining (21), (23) and (24) yields the charge density for $x \in \,]-a,+a[$

$$\xi = \frac{\tilde{V} \sigma_0}{\pi} \left(\frac{1}{x+a} - \frac{1}{x-a}\right) . \qquad (25)$$

Upon integrating this density distribution, the total charge on the sensor surface and, consequently, the probe capacitance in air may be calculated. We find

$$C_0 = \sigma_0 \, \ell = \sigma_0 \frac{2 \, d}{\pi} \, \ell \mathrm{n}[\frac{a+b}{a-b} \frac{a-c}{a+c}] . \qquad (26)$$

This calculation also allows us to estimate the height of the measurement volume, which, in a homogeneous medium, is bounded by the extreme field lines emanating from edges of the sensor surfaces. From Eq. (22), the height of the outermost field line is

$$h = (a^2 - c^2)/2c . \qquad (27)$$

Because, as this Eq. indicates, increasing the dimension c reduces h, it is natural to bring the edge of the sensor surface closer to the singularities at $x = \pm a$ in order to confine the measurement volume further. However, increasing c makes it more difficult to control the value of the capacitance. In the extreme situation where b and c nearly equal a, the value of the capacitance is very difficult to predict, as it becomes excessively sensitive to small excursions in the values of c/a and b/a.

Employing an analysis similar to that of Louge, et al (1996), we minimized the sensitivity of the instrument to dimensional excursions that may result, for example, from manufacturing tolerances or deterioration of its front surface. To achieve this, we prescribed $(b/a) \approx 0.29 \, (c/a) + 0.70$. Then, using the smallest value of c that allowed adequate clearance between the two sensors, we adopted a = 5 mm, b = 4 mm and c = 1 mm.

In order to detect snow layers as thin as possible, we set the height of the sensor at the value that produced the minimum detectable capacitance of about 25 femtoF or $\ell = 2.8$ mm. From Eq. (21), the resulting measurement volume then penetrated a horizontal distance h = 12 mm into the pack while resolving layers of thickness d = 2.5 mm.

The processing electronics of the prototype consisted of a CAPACITEC low capacitance front-end preamplifier. Using a high speed 12 bit A/D converter, a micro controller/processor module controlled the oscillator frequency and our proprietary demodulation process, while producing phase information in real time using a separate detection circuit.

Following the first series of tests in Phase I and the user survey summarized in Appendix 3, we redesigned the tip of the sounding probe as shown in Fig. 11.
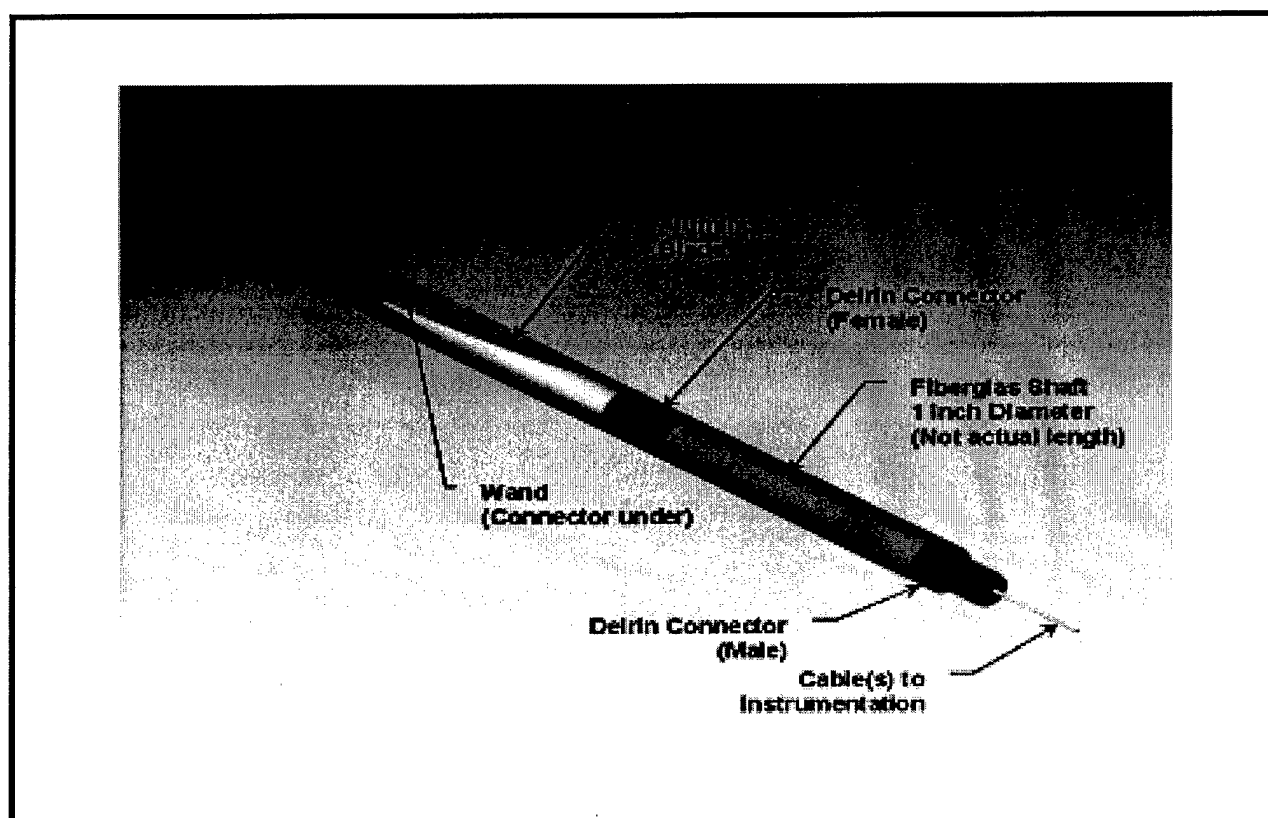
Fig. 11. Tip of the redesigned probe.

18

5. DIELECTRIC STRATIGRAPHY

The prototype and redesigned probes were tested in the mountain resort of Alta near Salt Lake City, Utah. This section summarizes the conditions and results of the tests. The latter were carried out in cooperation with the University of Utah, the Utah Department of Transportation and the Center for Snow Science at Alta, who provided logistical assistance and carried out complete snow profiles in adjacent pits. Figures 12 to 15 correspond to tests carried out in February, 1997 during Phase I with the amplifier at 15.6 kHz and the prototype of Fig. 9. Figures 16 and 17 show similar data for the amplifier at 3.9 kHz collected at Alta on February 23, 2001 near the Lower Guard Station with the redesigned probe of Fig. 11. For both amplifier frequencies, note the remarkable agreement between the density profiles measured in the pit and the density stratigraphy recorded by the probe.
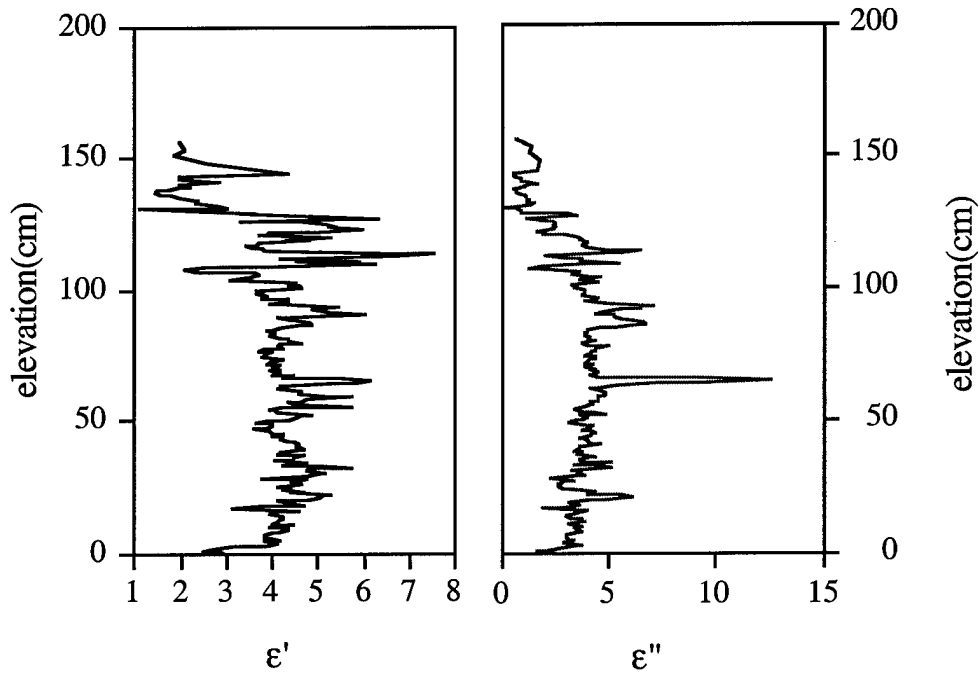
Fig. 12. Real and imaginary parts of the dielectric constant at 15.6 kHz versus elevation with origin is at the base of the pack.

19
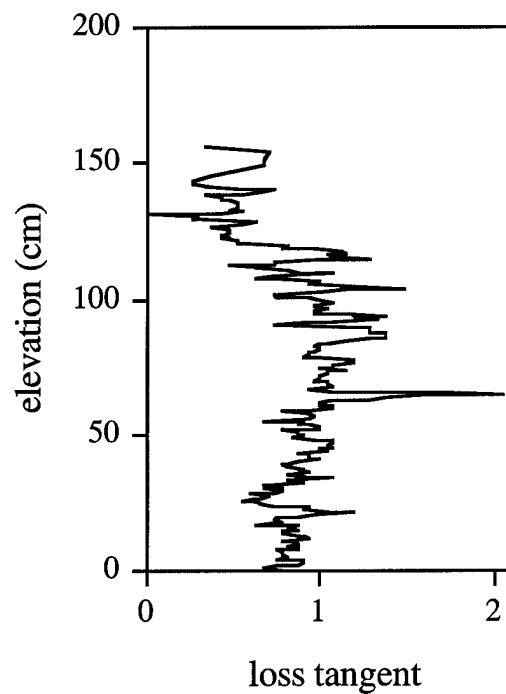
Fig. 13. Loss tangent versus elevation for the amplifier at 15.6 kHz.
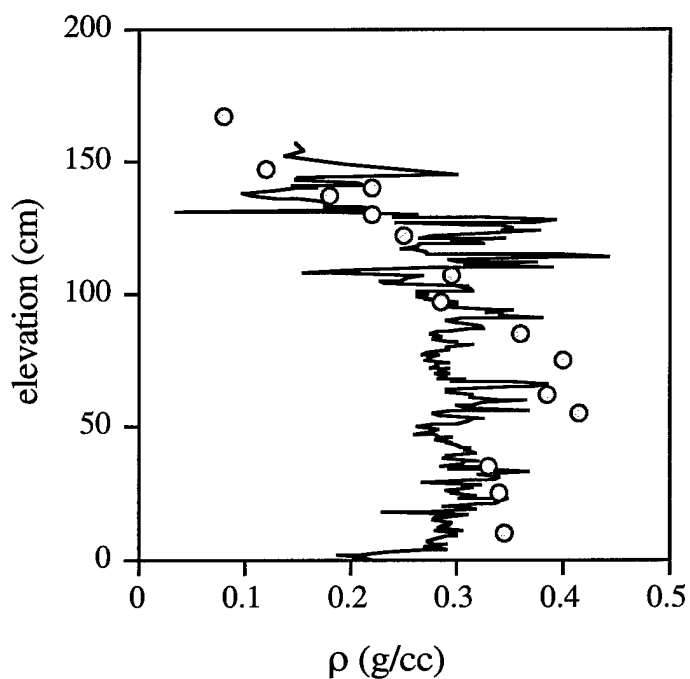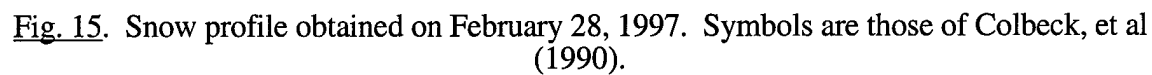

Fig. 14. Snow density versus elevation inferred from the sounding of Fig. 12 and the calibration of Fig. 5 (amplifier at 15.6 kHz). The line is the detailed sounding of the capacitance probe and the symbols are from direct density measurements carried out in an adjacent pit (Fig. 15).
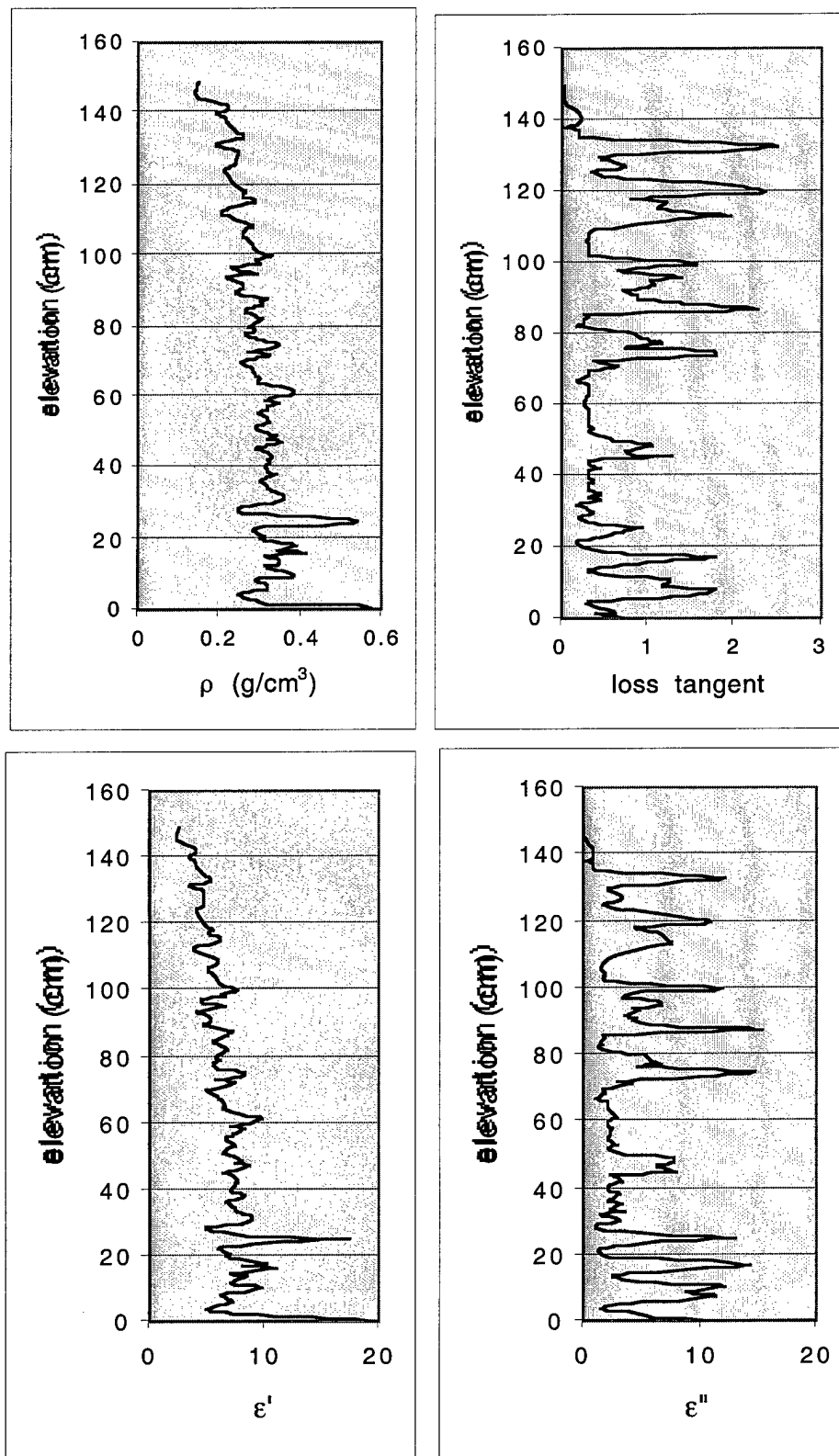
Fig. 15. Snow profile obtained on February 28, 1997. Symbols are those of Colbeck, et al (1990).

Fig. 16. Density, loss tangent, ε' and ε" stratigraphies for the soundings on February 23, 2001 near the Lower Guard Station using the amplifier at 3.9 kHz.
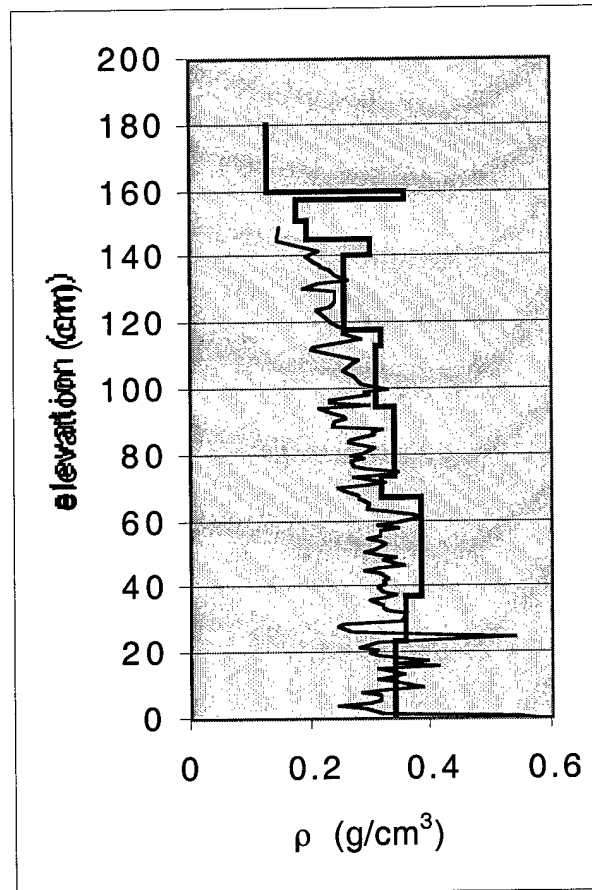
Fig. 17. Density stratigraphy for the pit dug on February 23, 2001 near the Lower Guard Station. The heavy line shows data from the snow pit and the thin line from the sounding probe.

As observed earlier, the loss tangent possesses a more contrasted stratigraphy at 3.9 kHz than at 15.6 kHz. This property can be exploited to identify layers that have previously been observed in a conventional excavation. To illustrate this, Fig. 18 shows density soundings obtained at two locations separated by about 2 m in the Alta Study Plot of the Utah DOT. Although both compare well with the manual data obtained from an adjacent pit, they show slightly different stratigraphies that betray subtle lateral changes in the snow pack. As Fig. 19 indicates, the loss tangent provide a sensitive signature for the various layers, which can then serve to indicate their depths in a entire basin. Figure 20 shows data from the conventional excavation carried out on February 24 at the Study plot.
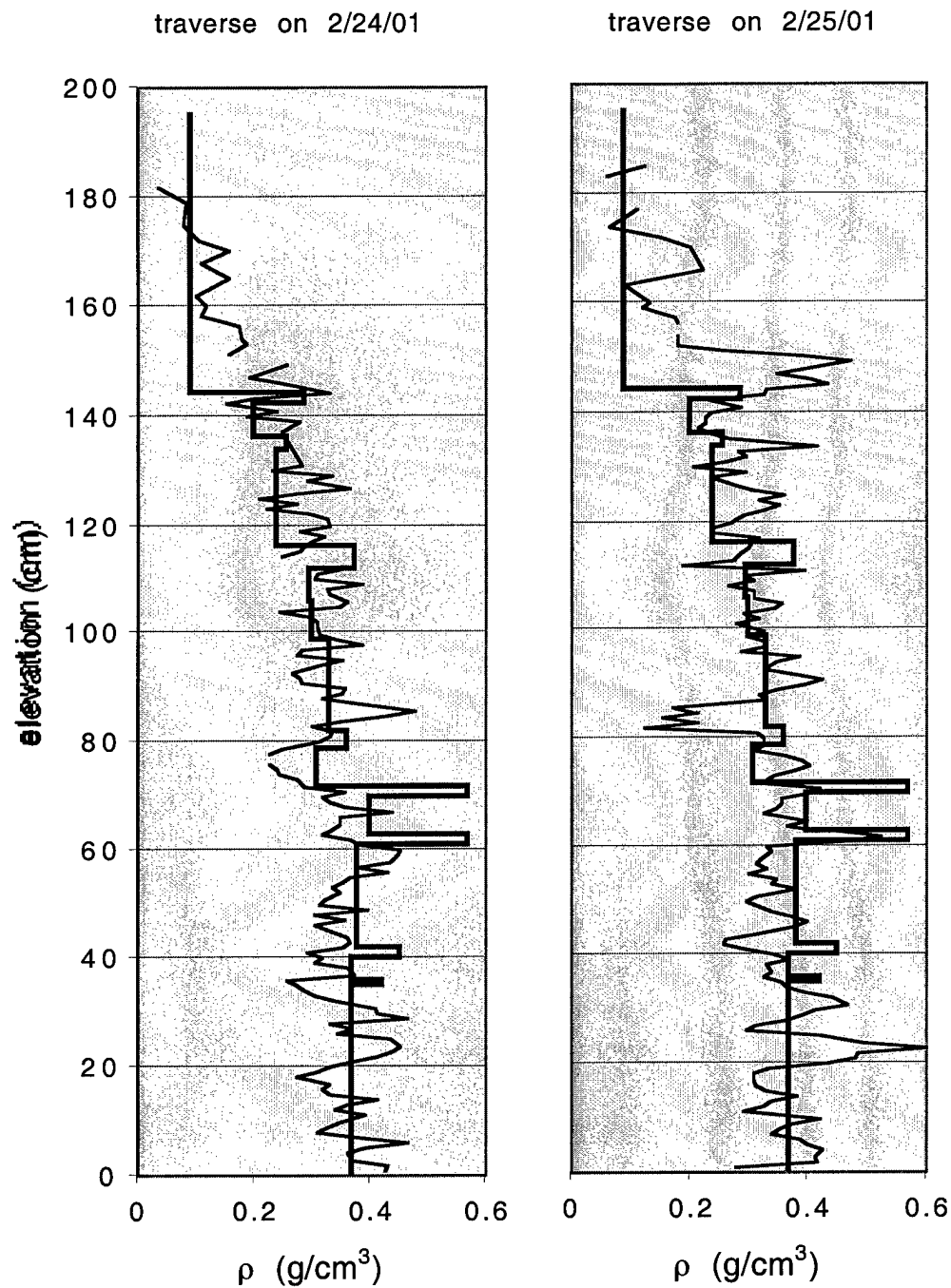
traverse on 2/24/01   traverse on 2/25/01

Fig. 18. Density stratigraphy at the UT DOT study plot. The thick line indicate the density profile measured with a conventional pit on February 24. Thins lines represent capacitance soundings. The sounding to the left was obtained with the amplifier at 3.9 kHz on February 24, while the one to the right was carried out about 2 m away on February 25.
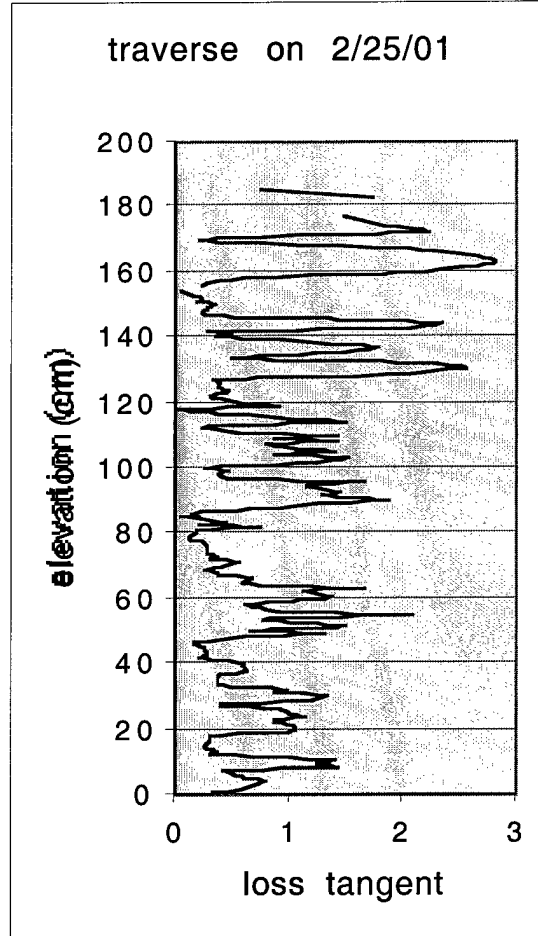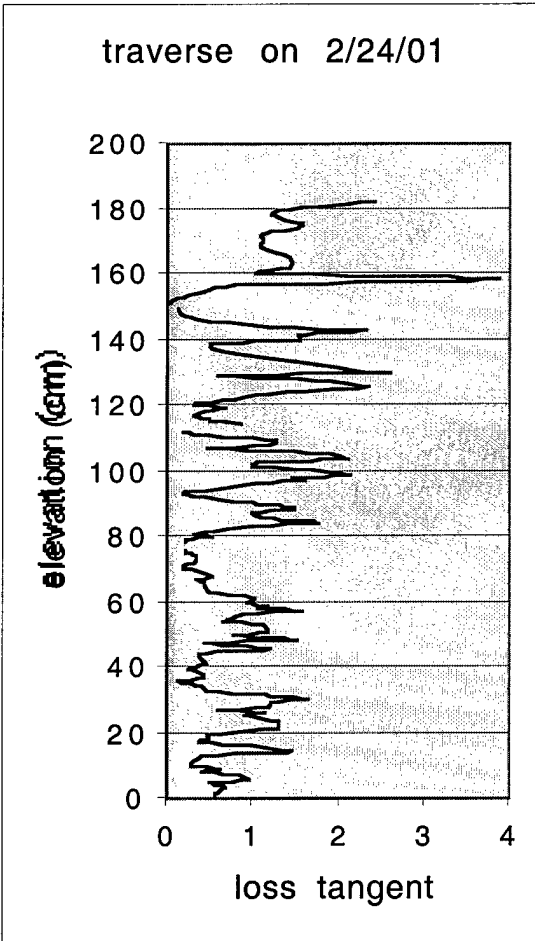
24

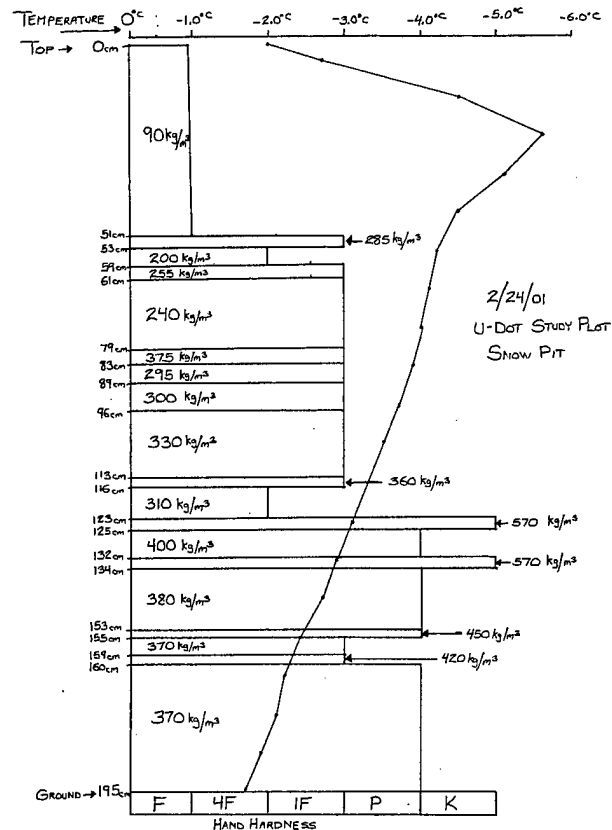Fig. 19. Loss tangent stratigraphy corresponding to the density soundings of Fig. 18.

Fig. 20. Snow profile obtained on February 24, 2001 in the UT DOT Study Plot.

Finally, Fig. 21 shows a series of depth profiles obtained near the "Supreme" avalanche corridor at Alta on December 16, 2001. The first two soundings demonstrate the reproducibility of our instrument. In contrast, the two eastern-most soundings indicate that the snow pack exhibited rapid horizontal variations. These variations are likely associated with rapid topographical changes. Figure 22 shows corresponding variations in the loss tangent.
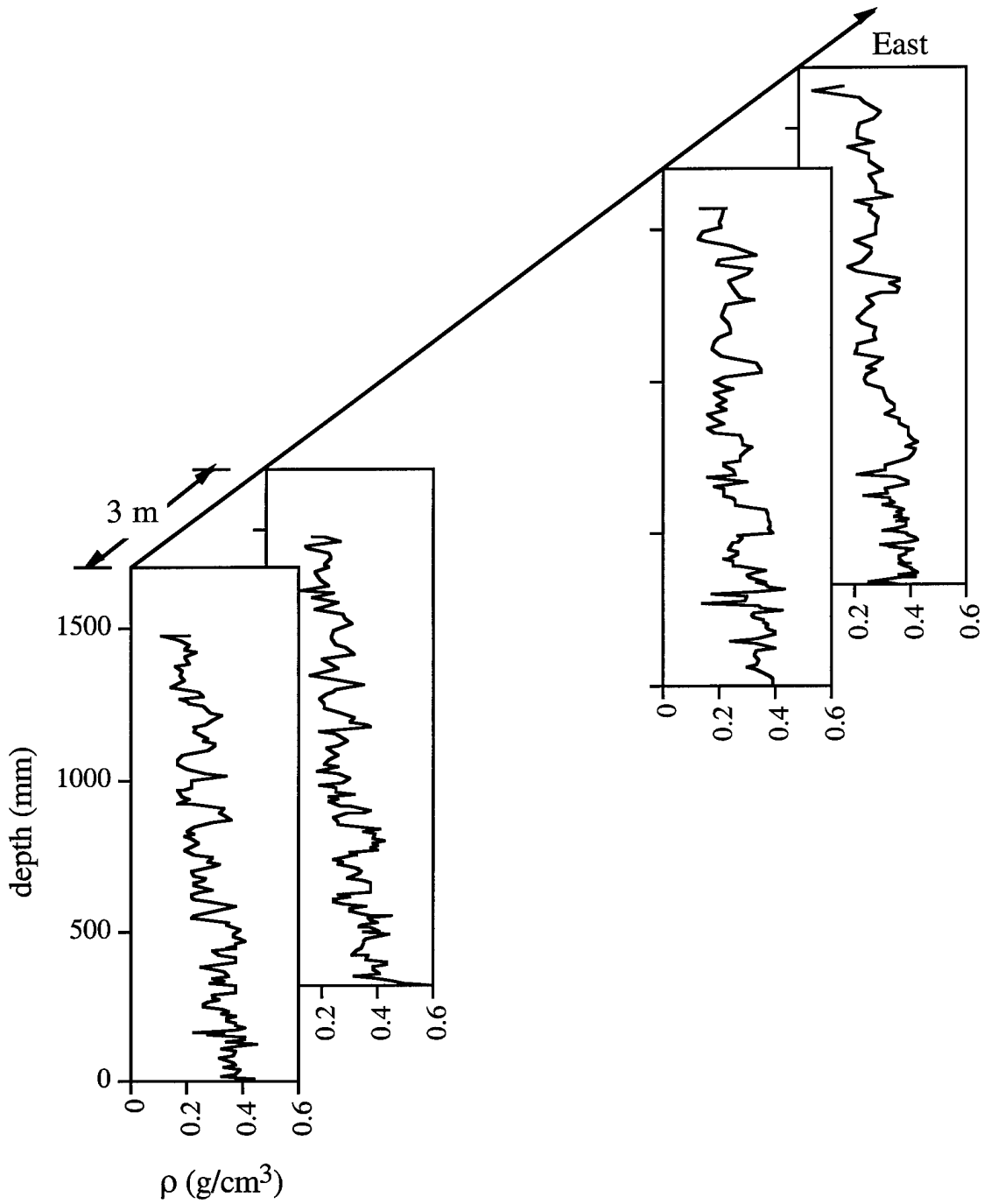
Fig. 21. Snow density depth profiles obtained on December 16, 2001. The oblique axis represents distance along a straight line pointed roughly eastward. From left to right, the four profiles are located at 0, 3, 12 and 15 m along that line.
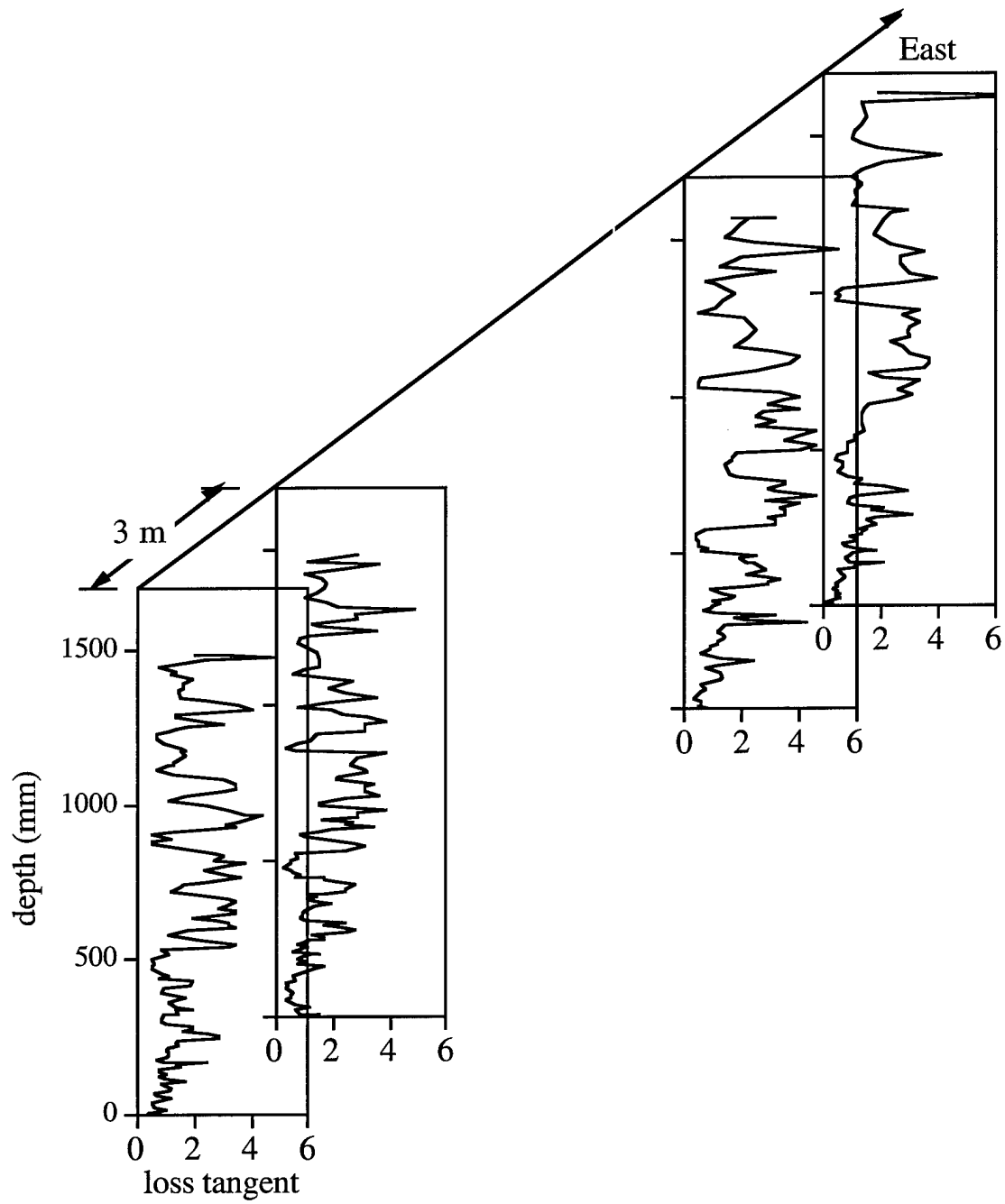
Fig. 22. Depth profiles of loss tangent obtained on December 16, 2001. For conventions, see Fig. 21.

6. TEMPERATURE STRATIGRAPHY

We have added a thermistor to the snow sounding probe to record the stratigraphies of temperature through the snow pack. Appendix 3 explains how the thermistor signal is generated and linearized using a half-bridge. In short, the circuit yields the following output voltage V:

$$V \text{ (volts)} = 0.1 \text{ } T(°C) + 2.027 \text{ (volts)}, \tag{28}$$

where T is the probe temperature in °C. The circuit achieves an accuracy and linearity better than 0.1°C over the range $-15° \leq T \leq +5°C$. Figure 23 compares the temperatures measured by the probe and recorded in a conventional pit excavation on the same day (Fig. 20). The two measurements agree within better than 0.5°C.
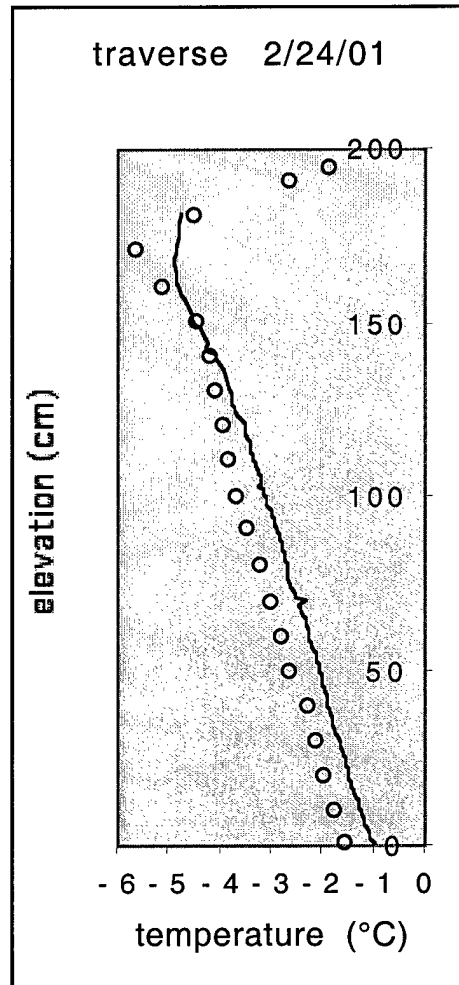
Fig. 23. Temperature stratigraphy obtained on February 24, 2001. The line is temperature recorded by the thermistor on the sounding probe. The symbols are data from the traditional excavation.

7. Depth Measurement and Data Acquisition

In its scientific and commercial models, the sounding probe features an automatic way to record depth in the snow pack. Although this convenience is not strictly necessary, our potential customers have generally expressed interest in this feature, as our Marketing Survey has revealed (Appendix 4).

The data is recorded by a data acquisition card (MyCorder DataStick http://www.datastick.com) on a Palm III (3Com -- http://www.palm.com). The system successfully acquired data down to temperatures of -19°C during our complete system tests carried out at Alta in December 2001. As temperature dropped, we simply adjusted the contrast on the Palm pilot screen to compensate for changes in the liquid crystal display. The system can acquire six voltage channels with 12-bit resolution either continuously or when triggered by the user.

The first voltage channel is dedicated to depth. To measure the latter, the shaft of a US Digital rotary encoder is connected to a neoprene-coated wheel in permanent contact with the lance. The contact is maintained by constraining the vertical lance to move between a fixed pulley and a spring-loaded wheel. The encoder, wheel and pulley are mounted on a plate that is laid on the snow pack. The lance traverses the plate through a hole (Fig. 24). The probe electronics are accommodated in the same rack that is used for the measurements of dielectric constant and temperature.

In the December 2001 tests, we employed a neoprene-coated aluminum drive roller of 2.125" nominal diameter (53.5 mm actual) model 60885 K25 from McMaster-Carr [www.mcmaster.com] and maintained in contact with the 1" OD lance using a Dynapar [1 800 922 1103] Pivot Mounting Bracket model 14005740000.

The encoder is a sealed rotary optical shaft encoder model H1-360-HS from US Digital [360 260 2468 - www.usdigital.com]. This encoder provides in-phase and quadrature pulses at a rate of 360 pulses per revolution. Thus, the vertical resolution of the system is $\Delta z = (2\pi/360) D_{roller}/2 = 0.47$ mm, where D_{roller} is the diameter of the drive roller. The quadrature signal of the encoder is converted to a voltage using a US Digital EDAC-NP converter (http://www.usdigital.com/products/edac) that is fed to the Palm Pilot data acquisition card.[1]

---

[1] The EDAC has dip switches set for (x4, count up, ignore reset, and range 0-4.095 Volts). The user resets the EDAC with a manual pushbutton prior to starting a traverse. If the depth displacement exceeds the range of the EDAC (~1.9 meters) the output "wraps" to zero and continues to increment. This discontinuity is removed in post-processing to extend range.
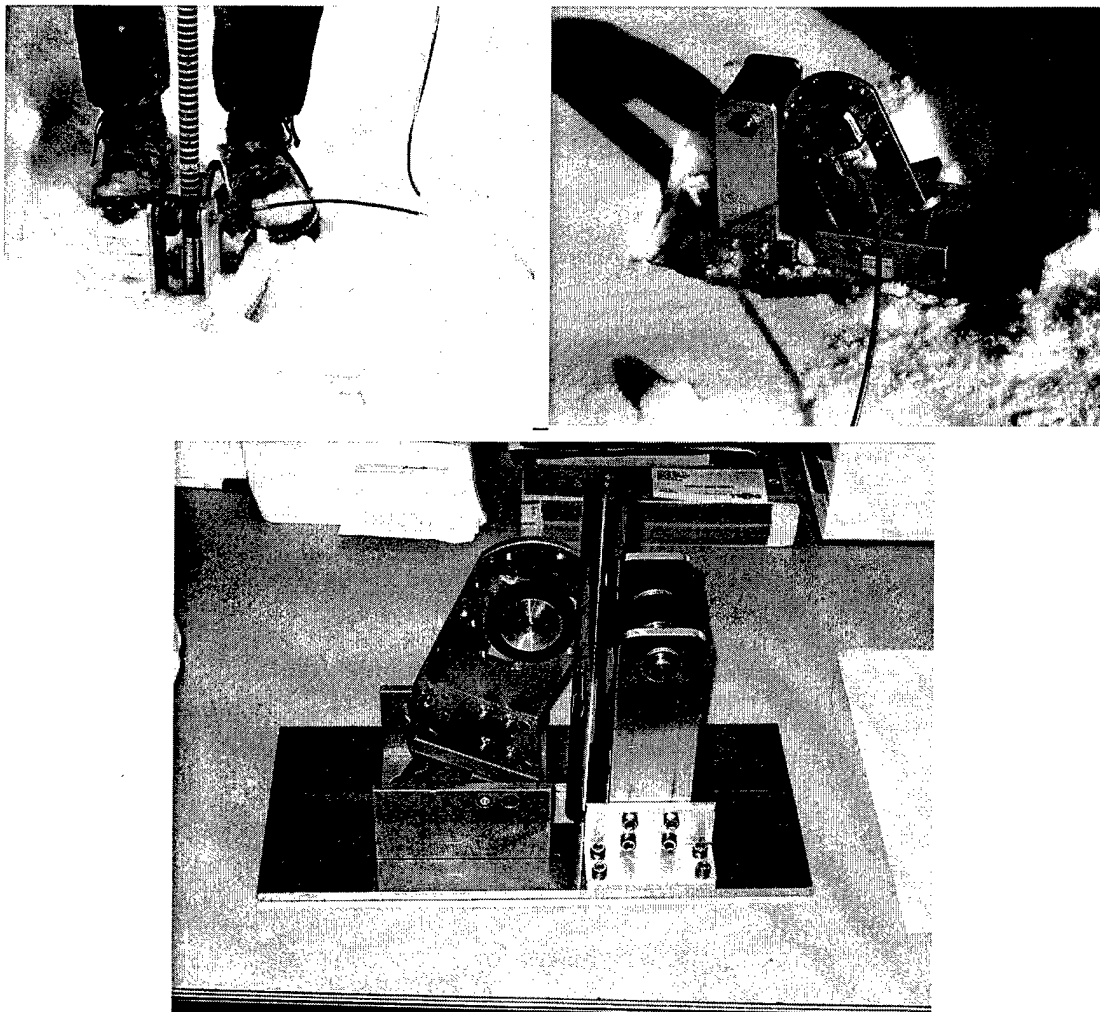
Fig. 24. Pictures of the depth measurement device.

The data acquisition card also acquires a temperature voltage, which is converted to an actual temperature using Eq. (28), and two voltages, V_{real} and V_{im}, from which we extract the voltage output V and the phase ϕ between oscillator and guard using:

$$V_{real} = V \cos\phi \qquad (29a)$$

and

$$V_{im} = V \sin\phi . \qquad (29b)$$

In future, the remaining channels could also carry voltage information on infrared backscattering.

31

In the December 2001 tests at Alta, we demonstrated how quickly the snow pack could be penetrated. Figure 25 shows a typical depth time-history. The user completed the entire 1200 mm traverse in a mere 25 seconds.

However, because our system has a limited acquisition bandwidth, the traversing speed ultimately depends upon the degree of resolution that the user expects. In particular, we set a cut-off frequency of approximately 25 Hz to minimize the noise in V_{im} and V_{real}, while keeping a reasonable acquisition speed. In order to resolve layers of 0.5 mm thickness, this frequency then limits the continuous penetration speed to 0.5mm x 25Hz ≈ 12.5 mm/sec. In this case, each meter of snow pack would be penetrated in 80 sec with a 0.5 mm resolution. If the user desires a greater penetration speed, we can design a system with a greater acquisition bandwidth in the future.
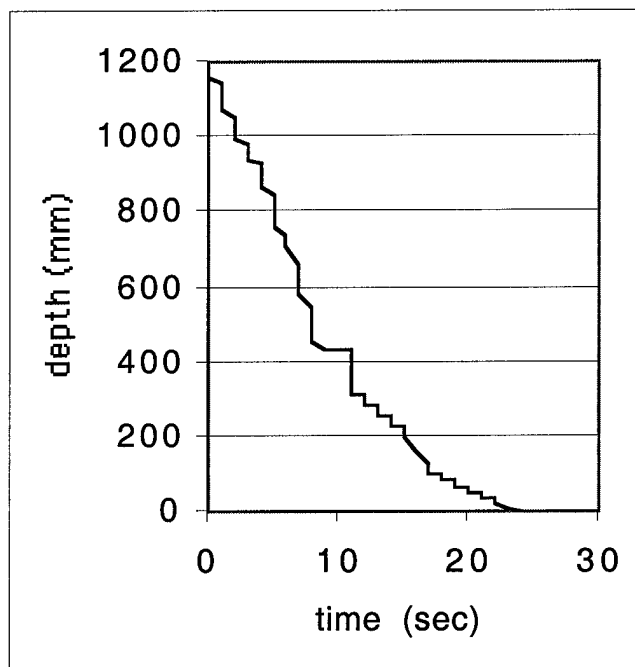

Fig. 25. Depth time-history in a typical penetration of the snow pack. Because the frictional force on the lance increases with depth, the penetration speed decreases with time.

We have also benchmarked the depth recording system against a linear encoder consisting of a magnetic strip glued to the side of the lance. The strip (magnetic tape PEMB2040) possesses thin magnetized regions that are detected by a fixed head (PEMIX3) mounted on the horizontal plate laid on top of the snow pack. The system is distributed by NorthStar (www.northstar-tec.com - 1 800 326 6216). The resolution is user-selectable between 5μm to 1mm. We tested the system in a cold room at -32°C. The

resolution of 0.1mm was maintained down to such temperatures. Disadvantages of the magnetic strip are a relatively high price (strips cost $117/m; the head and cable are $500) and inconvenience: the strip cannot operate properly if its distance to the head is beyond 2.5mm.

8. FEASIBILITY OF OPTICAL MEASUREMENTS

The authors are grateful to Professor Jimmie Dent of the Montana State University for helpful discussions and for suggesting to use the OpTek chip.

We have investigated the feasibility of inferring grain size from the backscattering of infrared (IR) light at 930 nm using a commercial chip (OpTek OPB706C) consisting of rectangular IR light-emitting diode parallel to a rectangular phototransistor detector. The two rectangles have nominal dimensions of 1.3 mm x 3.9 mm. The centerline of the two rectangles are separated by 2.2 mm.

The chips are manufactured by OpTek Technologies, Inc. [www.optekinc.com - Carrollton, TX (214) 323 2200]. Appendix 5 outlines our measurements of their optical characteristics. In summary, the photodiode has an active rectangular area of 1.3 mm width and 1.5 mm height emitting light in a narrow beam with intensity distribution $I (\cos\theta)^n$, where I is a constant power per unit area and unit solid angle, θ is the angle of the light ray from the normal to the chip, and $n \approx 13$. The phototransistor detects IR light returning to an active rectangular area of 1.3 mm width and 3.1 mm height. Note that the active areas of the phototransistor and light-emitting photodiode are both smaller than the values printed in the specifications.

The chips are incorporated in a simple resistor circuit sketched in Fig. 26. To insure linearity of the photodetector, resistor values can be increased until the output voltage is well below the 5 V supplied to the circuit.
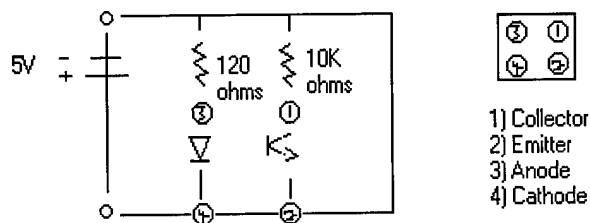

Fig. 26. Typical circuit with the OPB706C.

To evaluate the effect of grain size on the response of the chip, we carried out a series of Monte-Carlo simulations and experiments where snow grains were represented by glass beads of various sizes. Appendix 6 describes these simulations. As Fig. 27 shows, the measured backscattered light compares reasonably well with the predicions of the simulations at a particle volume fraction of 50%. In addition, Fig. 28 indicates that the dependence of backscattered light intensity on solids volume fraction is less pronounced than the corresponding dependence on particle size. Consequently, it seems possible to employ the OpTek chip as a method to evaluate grain size without introducing excessive corrections for snow density.
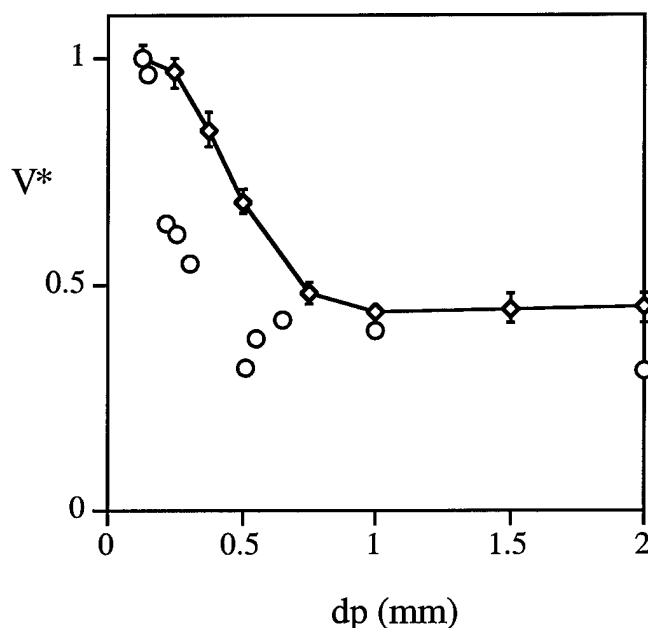
Fig. 27. Dependence of the backscattered light intensity on the particle diameter for loosely packed glass spheres. The intensity is made relative to its value for a sphere diameter of 0.125 mm. The circles are measurements. The diamonds are average results from 20 simulations at a solid volume fraction of 50%. Straight lines join the simulation points. The error bars represent the sample standard deviation from the 20 simulations.
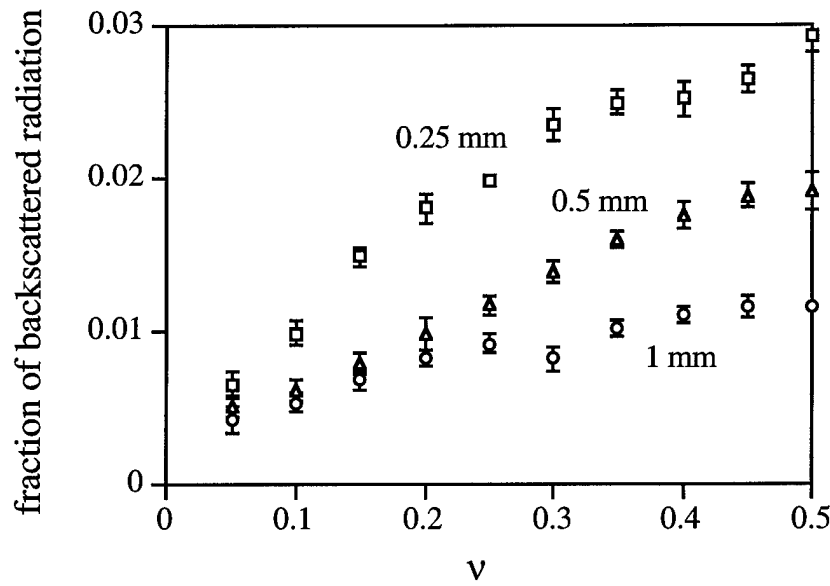
Fig. 28. Fraction of light intensity returned to the photodetector versus solid volume fraction. The squares, triangles and circles represent glass spheres of 0.25, 0.5 and 1 mm diameter, respectively. The bars represent the error calculated from averaging results from 20 simulations at 80% degree of confidence.

However, as Fig. 27 shows, the OpTek chip becomes relatively insensitive to grain size for d > 1 mm, thus limiting its usefulness for detecting relatively large grains. We then used the simulations to prescribe chip dimensions that would yield a greater range of detectable snow grain diameters. Figure 29 shows the result of changing the distance between the centerlines of the light-emitting photodiode and the photodetector. If the distance between the two rectangles is reduced, then the amount of backscattered light becomes more sensitive to grain size. Ultimately, if we were able to make the emitter and detector coincide (which is impossible without coupling the light into a single optical fiber and exposing the latter to snow), the dependence on grain size would be the sharpest. Lischer and Louge (1992) discussed this dependence for a multimode optical fiber. As Fig. 29 shows, an optimum dimension between photodiode and photodetector is on the order of 1.7 mm, which requires the placement of the two rectangles roughly side-by-side. This would make the backscattered radiation signal sensitive to grains as large as 3 mm. Because this can only be achieved by redesigning the chip, we decided not to implement this measurement in Phase II.
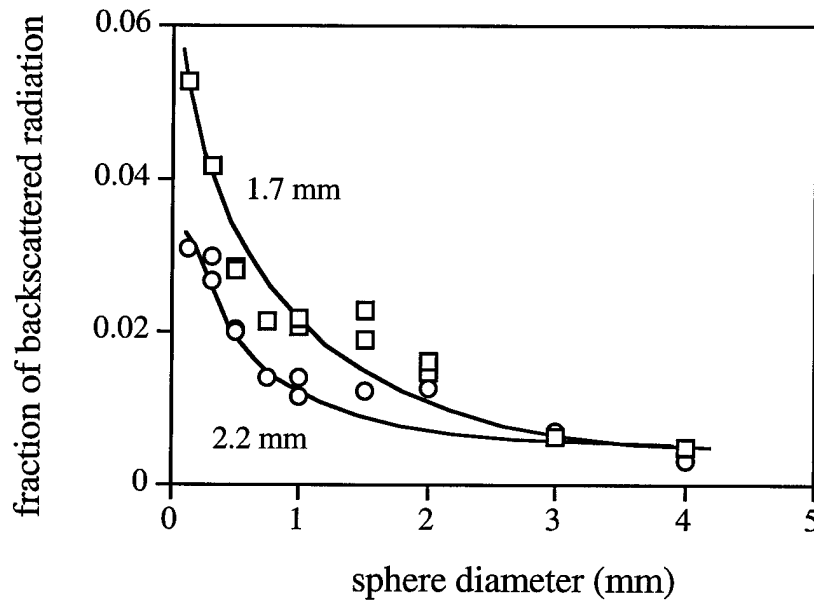
Fig. 29. Fraction of light intensity returned to the photodetector versus diameter of glass spheres. The circles correspond to the current separation of 2.2 mm between the centerlines of the light-emitting photodiode and the photodetector in the OpTek chip. The squares represent a hypothetical chip with a smaller separation distance of only 1.7 mm.

10. ACKNOWLEDGMENTS

9. REFERENCES

Bayvel, L.P. and Jones, A.R. (1981) *Electromagnetic Scattering and Its Applications* (Applied Science Publishers, London), p. 66.

Brown R.L. and Dent J.D. (1996) "Research Priorities in Snow Mechanics and Snow Physics," *US Army Research Office*.

Denoth A. , A. Foglar, P. Weiland, C. Mätzler, H. Aebischer, M. Tiuri and A. Sihvola (1984) "A comparative study of instruments for measuring the liquid water content of snow," *J. Appl. Phys.* **56** (7), 2154-2160.

Deirmendjian, D. (1969) *Electromagnetic Scattering on Spherical Polydispersions* (American Elsevier Publishing Company, New York), p. 10.

Kerker, M. (1969) *The Scattering of Light* (Academic Press, New York), p. 106-107.

Kuroiwa D. (1967) "Snow as a material. Chapter J. Electrical Properties of snow," in: Cold Regions Science and Engineering, Part II, Section B: Physical Sciences, US Army Materiel Command, Cold Regions Research and Engineering Laboratory, Hanover, NH, pp. 63-79.

Lischer, D.J. and Louge, M. (1992) "Optical fiber measurements of particle concentration in dense suspensions: calibration and simulation," *Applied Optics* **31**, 5106-5113.

Louge M.Y., Foster R.L., Jensen N. and Patterson R. (1998): "A Portable Capacitance Snow Sounding Instrument," *Cold Regions Science and Technology* **28**, 73-81.

Louge M. and M. Opie (1990) "Measurements of the effective dielectric permittivity of suspensions," *Powder Tech.*, **62**, 85-94.

Louge M.Y., Steiner R., Keast S.C., Decker R., Dent J. and Scheneebeli M. (1997) "Application of Capacitance Instrumentation to the Measurement of Density and Velocity of Flowing Snow," *Cold Regions Science and Technology*, **25**, 47-63.

Louge, M., Tuccio, M., Lander E. and Connors, P. (1996) "Capacitance Measurements of the Volume Fraction and Velocity of Dielectric Solids Near a Grounded Wall," *Rev. Sci. Instrum.* **67** (5), 1899-77.

Probert-Jones, J.R. (1984), "Resonance Component of Backscattering by Large Dielectric Spheres," *J. Opt. Soc. Am.* **1**, No. 8, 822-830.

Warren, S.G. (1984) "Optical constants of ice from the ultraviolet to the microwave," *Applied Optics* **23**, 1206-1225.

APPENDIX 1 - CHARACTERISTICS OF THE CAPACITANCE AMPLIFIER AT 3.9 KHZ

Accurate measurements of the dielectric properties of the snow pack require an understanding of the response of the capacitance amplifier. To determine its operational parameters, we conducted a series of bench tests using a known capacitance standard.

We first established the linear range of the amplifier. In this range, the output voltage of a pure capacitance is inversely proportional to C. Generally, the amplifier is linear when $0 < 1/C \leq (1/C_{tr})$, where the minimum capacitance C_{tr} typically decreases with decreasing values of the oscillator voltage v_1 (or, equivalently, with decreasing values of the decimal gain of the digital signal processor). Thus, one may be tempted to decrease v_1 until the snow probe has a capacitance at least equal to C_{tr}.
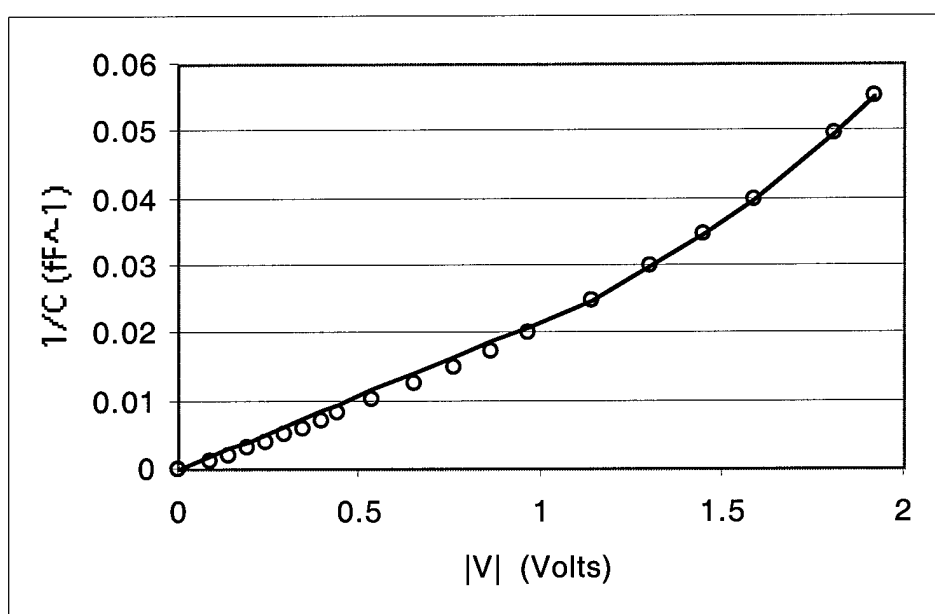

Fig. A1. Best fit of the inverse capacitance versus voltage relation in Eq. (A1) for the 3.9 kHz amplifier operating at a decimal gain of 10.

However, because the vertical resolution of the snow probe sensor must be narrow, its capacitance is relatively small (25 fF). Consequently, if we insisted upon a linear dependence of the output voltage on 1/C, we would require a small value of v_1, and consequently a small output voltage with low signal-to-noise ratio. With the Capacitec PC-501 amplifier at 3.9 kHz, a compromise is to use a gain of 10 leading to $C_{tr} = 40.1$ fF. In this case, although the snow probe operates within the non-linear range when it is immersed in air or in very light snow, its output is linear for most snows of interest. Even when the amplifier is non-linear, it is possible to extract information on the impedance of an unknown sample using the empirical fit

$$\frac{|Z|}{|Z_{tr}|} = \frac{C_{tr}}{C} = \frac{V}{V_{tr}} \qquad\qquad \text{for } C \geq C_{tr} \text{ (linear region)} \qquad \text{(A1a)}$$

and

$$|Z| = \frac{1}{2\pi fC} = \frac{1}{2\pi fC_{tr}} - \frac{1}{2\pi fC_{\infty}} \ln[1 - \frac{V - V_{tr}}{V_{\infty}}] , \qquad \text{for } C \leq C_{tr} \text{ (non-linear region).} \quad \text{(A1b)}$$

where $C_{\infty} = 20.3$ fF, $V_{tr} = 1.15$ V, and $V_{\infty} = 1.69$ V (Fig. A1).

Because the amplifier at 3.9 kHz exhibits non-linear behavior, we must rely on an absolute voltage measurement to infer the dielectric constant of a snow sample, rather than simply forming the relative voltage ratio of Eq. (8) to do so. Unfortunately, we have observed that the voltage of the snow probe in air can occasionally change as the amplifer gain, and thus the oscillator voltage, drifts slightly. However, because the voltage output of the snow probe is proportional to the amplifier gain, small corrections of the voltages V_{real} or V_{im} can be carried out as follows,

$$V_{real \text{ or } im}^{rescaled} = \frac{V_{real \text{ or } im}^{snow}}{V_{air\_before\_sounding}} V_{air,ref} , \qquad\qquad \text{(A2)}$$

where $V_{air,ref} = \sqrt{V_{real}^2 + V_{im}^2} = 2.18$ V is the voltage output of the snow probe in air measured in the laboratory, V_{snow} is the voltage measured in the snow soundings, and $V_{air\_before\_sounding} = \sqrt{V_{real}^2 + V_{im}^2}$ is the voltage recorded with the probe in air just before the soundings. The rescaled voltage can then be used to infer the probe's impedance in the presence of snow using Eq. (A1).

Interpretation of the phase information recorded with the sounding probe requires the knowledge of the constants $m(1+\delta H)$ and $n(1+\delta H)$ in Eqs. (14) and (15). We measured these constants by connecting the amplifier to the circuit of Fig. 2 and by recording the resulting phase and output voltage. In that circuit, we connected a guarded 200 MΩ resistance in parallel with a standard reaching capacitances in the range $18 \leq C \leq 860$ fF. The standard is a guarded capacitance probe with a sensor of area A parallel to a grounded surface. Its capacitance is adjusted by changing the distance d between ground and sensor,

$$C = \sigma_0 \frac{A}{d} , \qquad\qquad \text{(A3)}$$

where $\sigma_0 = 8.854 \times 10^{-12}$ F/m is the dielectric permittivity of free space.
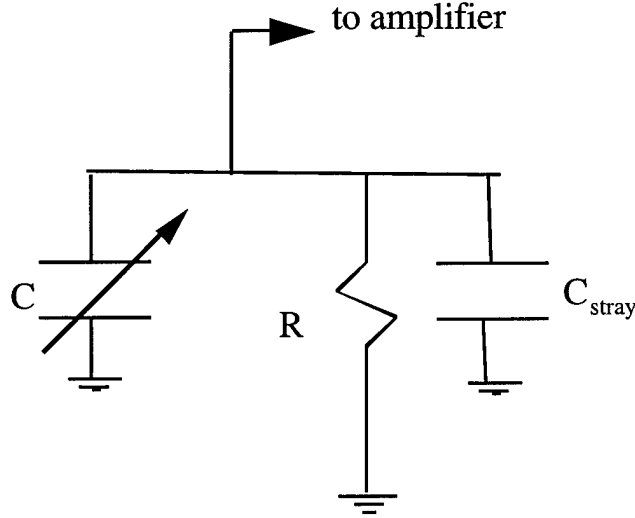
Fig. A3. Equivalent test circuit

Unfortunately, this test configuration is not as ideal as it appears. In fact, the guarded resistor box introduces a substantial stray capacitance, which arises from distortions of the electric field within the box. The equivalent circuit is sketched in Fig. A3. In this circuit, because the pattern of electric field lines changes with the voltage magnitude of the guard, C_{stray} is, to a good approximation, proportional to C. Then, the two capacitances C and C_{stray} are *both* inversely proportional to the distance d between sensor and ground. Equivalently, the two capacitances in parallel behave as if the capacitance standard had a larger sensor surface area A'>A. In the linear range of the electronics, the ratio of the voltage in air at a distance d_0 in the absence of R to the voltage in air at a distance d in the presence of R is then

$$\frac{V(d;R\neq\infty)}{V(d_0;R=\infty)} = (\frac{d}{d_0})\,(\frac{\ell_0}{\ell_1})\,\frac{1}{\sqrt{1+(\frac{d}{\ell_1})^2}} \tag{A4}$$

where $\ell_1 \equiv 2\pi f R \sigma_0 A'$, $\ell_0 \equiv 2\pi f R \sigma_0 A$, and f is the frequency of the oscillator. The corresponding phase ϕ recorded *from* the oscillator *to* the guard voltages* is

$$\tan\phi = \frac{n(1+\delta H) - m(1+\delta H)\,(\ell_1/d)}{R+m(1+\delta H)+n(1+\delta H)\,(\ell_1/d)}, \tag{A5}$$

We determined the constants $m(1+\delta H)$ and $n(1+\delta H)$ by fitting measurements of $V(d;R\neq\infty)$, $V(d_0;R=\infty)$ and $\tan\phi$ to the model of Eqs. (A4) and (A5). For best accuracy, we also fitted ℓ_0 and ℓ_1 for each test at a given oscillator amplitude. As Figs. A4 and A5

---

* Note that it is important to record the proper sign of the phase lag ϕ. In the current design, the amplifer features an output that is proportional to the conjuguate of the oscillator signal. Thus, the phase lag *from* this available output *to* the guard voltage is currently -ϕ.

illustrate, the resulting fit, which assumes m(1+δH) = 20 MΩ and n(1+δH) = 416 MΩ, captures well the phase and voltage of these tests over a wide range of conditions.
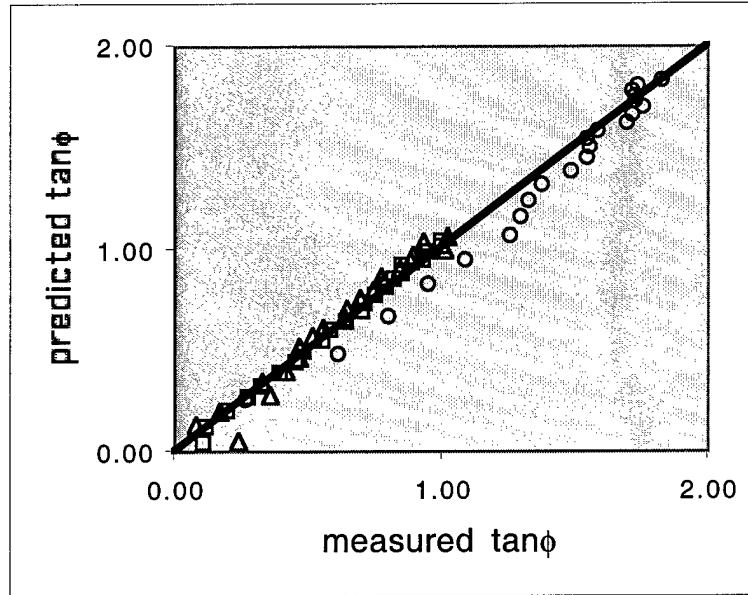
Fig. A4. Values of tanφ predicted by the model of Eqs. (A4) and (A5) versus measured values for the 3.9 kHz electronics. The circles represents tests with a decimal amplifier gain of 21 and a capacitance standard with a circular sensor of 13 mm diameter. The squares are for a gain of 43 and a sensor of 25 mm diameter. The triangles are for a gain of 21 and a diameter of 25 mm. The straight line denotes a perfect fit.
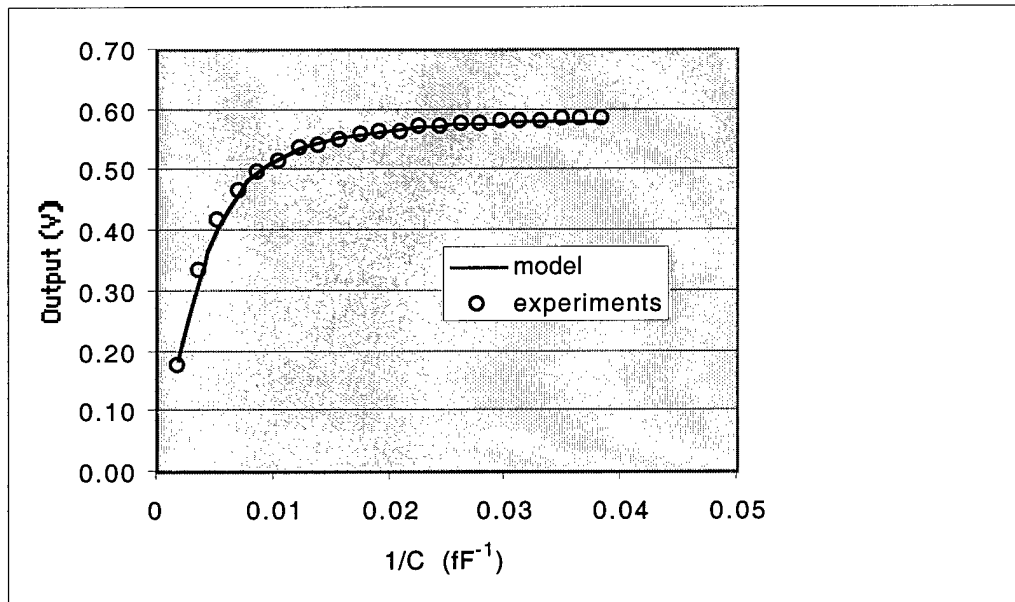
Fig. A5. Amplifier output predicted by the model of Eqs. (A4) and (A5) versus measured values for the 3.9 kHz electronics. For symbols, see Fig. A4. The line is the prediction of the model.

41

APPENDIX 2 - SNOW RESPONSE TO THE CAPACITANCE AMPLIFIER AT 3.9 KHZ

The empirical Eqs. (A1), (A2) and (A5) can be used to extract the real part ε' and imaginary part ε'' of the effective dielectric constant of snow

$$\varepsilon_e = \varepsilon' - j\,\varepsilon'', \tag{A6}$$

where $j^2 = -1$. First, the observed voltage is rescaled using Eq. (A2) and the corresponding impedance is extracted from Eq. (A1). Then, assuming that the snow probe has a capacitance of 15.6 fF in air, the ratio of impedances yields the modulus of the snow dielectric constant:

$$\frac{|Z_{air}|}{|Z|} = \sqrt{\varepsilon''^2 + \varepsilon'^2} \equiv \sqrt{c} \tag{A7}$$

and the individual components are

$$\varepsilon' = \frac{-B + \sqrt{B^2 - 4AC}}{2A} \tag{A8}$$

and

$$\varepsilon'' = \sqrt{c - \varepsilon'^2}, \tag{A9}$$

where

$$A = 1 + \left(\frac{(m/n) + \tan\phi}{1 - (m/n)\tan\phi}\right)^2, \tag{A10}$$

$$B = 2\,\frac{[(m/n) + \tan\phi]\,b\,\tan\phi}{[1 - (m/n)\tan\phi]^2}, \tag{A11}$$

$$C = \left(\frac{b\,\tan\phi}{1 - (m/n)\tan\phi}\right)^2 - c,$$

$$b = [2\pi f C_0 n (1 + \delta H)]^{-1}, \tag{A12}$$

and C_0 is the capacitance of the probe in air.

The temperature measurement circuit is used to sense the approximate probe tip temperature. The sensing element is a fast responding thermistor. The signal conditioning electronics are optimized to give an approximate linear output at 0.1 Volts per degree over the sensing range of –15.0°C to +5.0°C relative to the nominal 0°C voltage output. For our current components, the latter is 2.027 Volts. This voltage offset depends on the absolute acuracy of the thermistor and of the reference resistor. It may be reduced by appropriate component selection.

The resistance profile for a typical thermistor is shown in Figure A6. This curve is generated from a YSI incorporated, thermistor number SP20627-503F using the Steinhart and Hart equation to obtain a non-linear fit in the region of interest,

$$1/T = A + B \ln(R) + C [\ln(R)]^3, \qquad\qquad (A13)$$

where T is degrees Kelvin, R is the resistance in Ohms and A=7.702 10^{-4}, B=2.301 10^{-4} and C=7.558 10^{-8} are constants. The selected thermistors have the advantage to be drop-in replaceable to within 2.6% of the specified resistance over the –15.0 to +5.0°C measurement range.
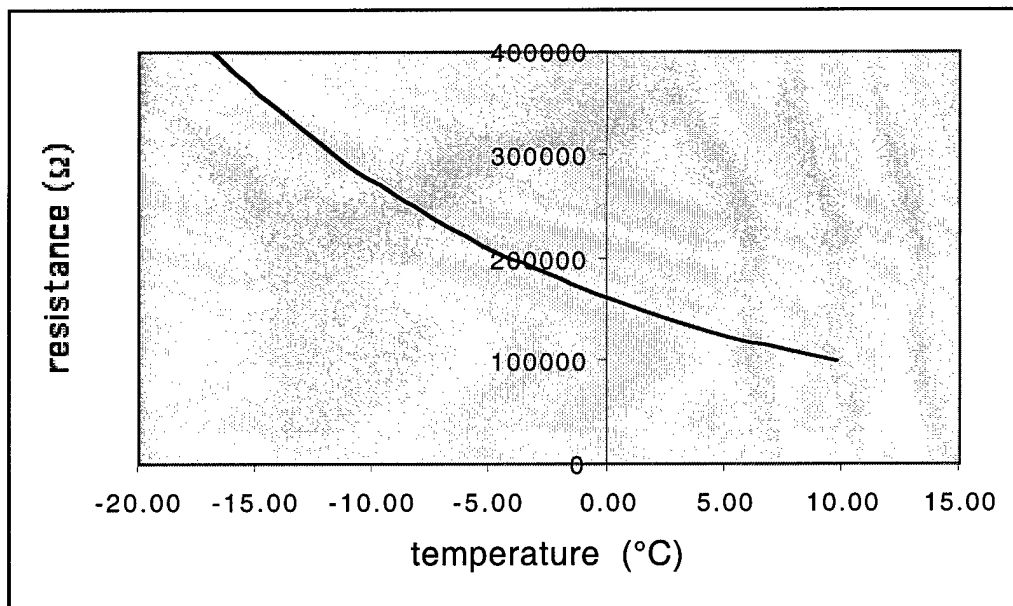

Fig. A6. Thermistor linearity profile

The resistance profile is non-linear due to the temperature profile and sensitivity of this class of temperature sensors. This thermistor comes in an 0805 package and is relatively responsive to thermal transients. The stand-alone sensor time constant is on the order of 8 seconds. The object of the conditioning circuit is to measure the response of the

thermistor and to generate an output that is relatively linear with temperature. The desired temperature accuracy, relative to the 0°C offset, is 0.1°C.

We achieve the linearization using a half-bridge circuit, which provide current to the thermistor and senses the resistance changes due to temperature (Fig. A7). The half-bridge circuit behaves in a non-linear manner, which complements the response of the sensor; the composite output provides a remarkably linear output around a reference point on the thermistor curve.
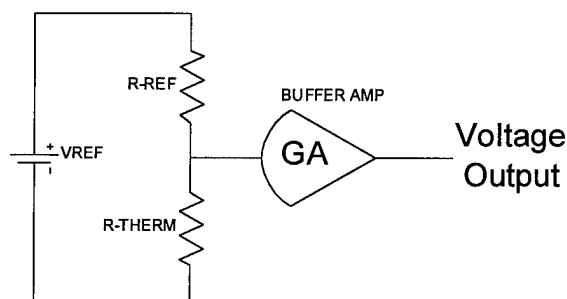

Fig. A7. Half-bridge measurement circuit. The buffer amplifier modifies the output of the half-bridge by offsetting and amplifying the signal linearly.

A voltage source (shown as a single cell) supplies a current to the reference resistor (R_{REF}) which is in series with the thermistor resistance (R_{THERM}). A reasonably high input impedance amplifier is used to measure the voltage division of the two resistances. Usually the source resistor is chosen to match the thermistor at a convenient temperature near the center of the desired temperature span. Here we have chosen 0°C as it is within band and at a convenient calibration point.

If the nominal reference resistance is R, and the change (vs. nominal) in the thermistor resistance is δR, the relative change in voltage output of the amplifier is

$$H(\delta R) = \frac{R+\delta R}{2R+\delta R} - \frac{1}{2} .$$
(A14)

Figure A8 shows the corresponding non-linearity of the half-bridge circuit.
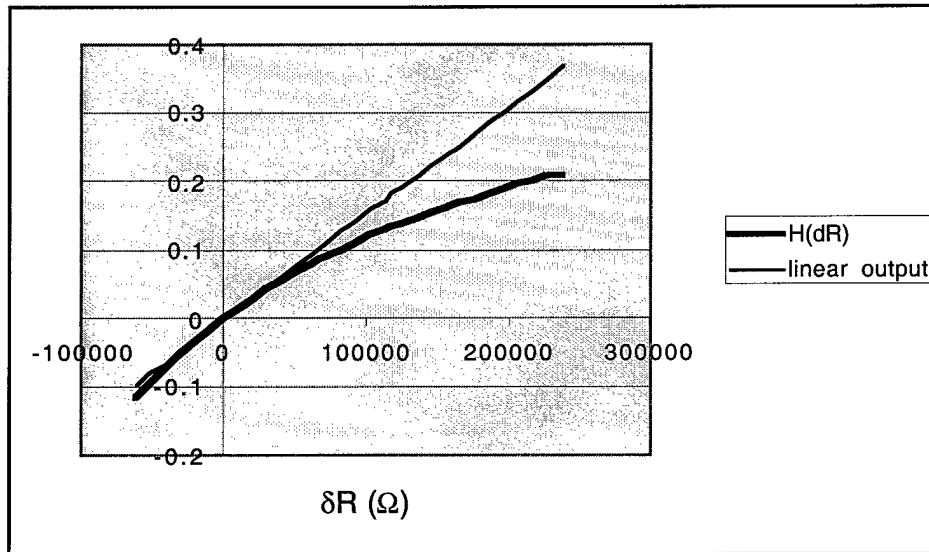
Fig. A8. Departure from linearity of the half-bridge. Relative change H(δR) in the output voltage versus change δR in the thermistor resistance.

This non-linearity helps linearizing the thermistor for negative values of resistance change (δR), and it is beneficial to skew the nominal resistance toward positive temperatures of the desired span. As Fig. A9 illustrates, the composite response of the thermistor circuit and the half-bridge is nearly linear. The output of the half-bridge is then passed through a linear circuit that transforms the voltage into

$$V \text{ (volts)} = 0.1 \ T(°C) + 2.027 \text{ (volts)}, \tag{28}$$

where V is the voltage acquired by the Palm Pilot.
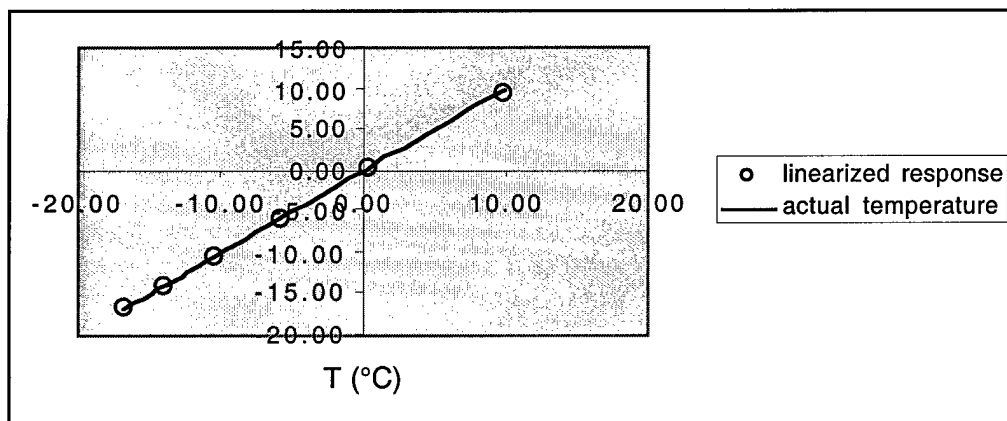
Fig. A9. Composite response of the thermistor and the half-bridge. The symbols represent temperatures inferred from the halfbridge output voltage v_o using $T = -78.5°C \ H(δR) = -78.5°C \ [v_o/V_{REF} - 1/2]$. The line is the actual temperature.

45

The fit's accuracy on the order of 0.1°C or less is adequate for the temperature range of interest (Fig. A10).
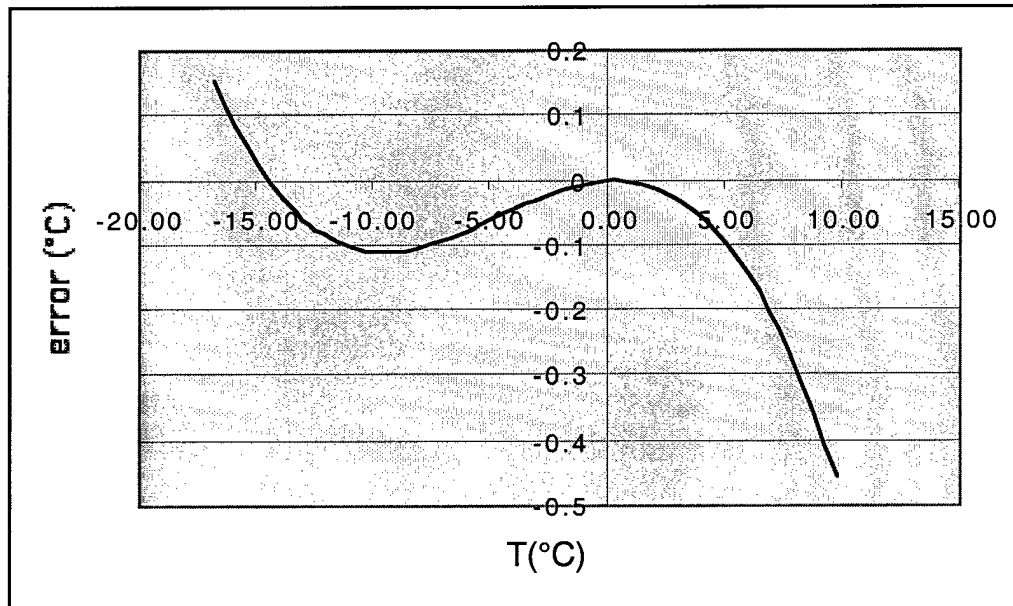

Fig. A10. Composite error of the thermistor and half-bridge.

Other errors, which are associated with conditioning the sensor temperature to a D.C. voltage, are caused by source resistor instability with ambient temperature, voltage source drift and amplifier zero drift (also with ambient or long-term). Using a worst-case analysis we estimate that these errors amount to less than 0.1% of full-scale over the desired 20 °C temperature span. Errors not directly related to the signal conditioning are shift due to heating while soldering the thermistor, self-heating, and transient errors due to the thermal time constants of the thermistor and surrounding thermal masses.

The thermistor circuit was tested by submerging the YSI thermistor in a distilled water bath. Both coated and un-coated thermistors were tested to make sure that conductivity of the water bath did not introduce additional errors. The water bath was surrounded by insulating material and stirred manually. The temperature was taken by three independent temperature measurement devices which all agreed to within 0.1 °C when the bath was stable. The bath temperature was lowered using ice and dry ice to obtain the various temperature readings or allowed to warm up from the freezing point. As Fig. A11 shows, the thermistor readings are in excellent agreement with the other temperature devices.

46
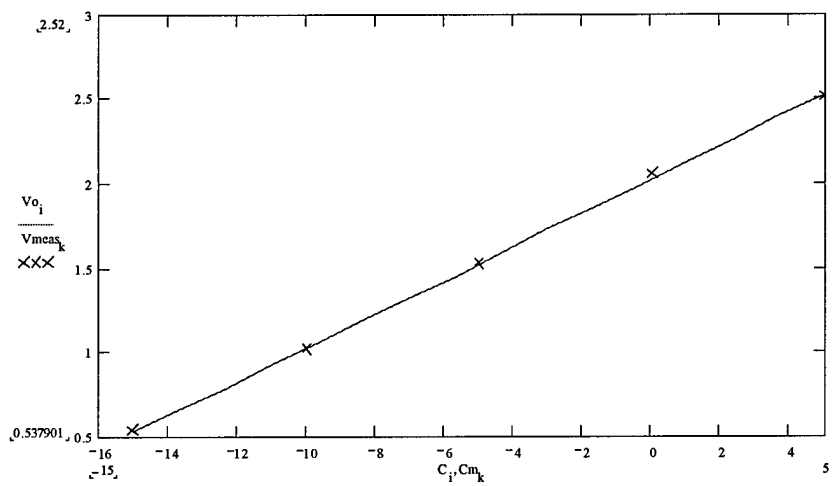
<u>Fig. A11</u>. Test results of the thermistor circuit. The crosses are thermistor readings plotted against temperatures measured by other means. The line signifies perfect agreement.

The following presentation is a summary of the Marketing Research efforts performed in conjunction with the development of the Capacitec Multi Parameter Snow Sounding probe.

This report will cover a chronological series of events that led to the latest product design and target market selections. These results were developed through a series of field trials, potential customer interviews and surveys as well as attendance at the International Snow Science and ARO Workshops.

The overall approach to marketing for the Snow Probe was to pursue a customer driven process. Unlike a product driven or engineering driven approach, this customer driven approach undertook to contact potential Snow Probe users in advance of final development to determine their specific wants and needs relative to the design of the Snow Probe.

Key Events and Schedule

Date	Event
1999/2000	Initial Snow Probe designed (see Figure 9) Customer survey developed and tested with key avalanche industry experts
October 2000	International Snow Science Workshop (ISSW) Big Sky, Montana. Capacitec circulated the survey during the conference and received direct feedback from attendees visiting their display at the conference.
Winter 2000	Additional surveys received from ISSW participants sent as a result of advertisements placed in Avalanche Review publication.
March 2001	ARO International Workshop on Ice & Snow Science Dartmouth College, NH. Results of customer survey were presented during the workshop. Feedback session held at the end of the presentation with all participants.
April 2001	Summary of additional results from the workshop
Summer 2001	Next generation Snow Sounding Probe redesigned based on inputs from summary of various potential customer inputs (Fig. 11).

December 2001	Tests of the snow probe system at Alta, Utah. Interview on Channel 4 "News4Utah" ABC affiliate in Salt Lake City. http://www.mae.cornell.edu/microgravity/snow_research.html
March 2002	Cover story of Sensors magazine http://www.sensorsmag.com/

Initial Market Segments

Customer feedback from the initial survey in 1999 drove the further development of three different versions of the first generation Snow Probe. The three product versions corresponded to three distinct market segments identified at that time.

An overview of these market segments is as follows:

CATEGORY I   Scientific/Academic Model
A.   Description – Combination instrument which measures relative snow density, temperature, grain size, wetness as a function of depth; portable but with time to set up for an "academic" study; may require multiple probes to meet all requirements.

B.   Users – Snow scientists, snow study institutes, university snow programs, hydrology and weather studies, State and Federal snow water resource management agencies.

CATEGORY II   Commercial Model
A. Description – A quickly deployable, portable, relative snow density and temperature instrument with a 2 – 3 meter depth probe and optional wetness and grain size; instrumented shovel configurations available where deep pits are always dug.

B.   Users – Ski area avalanche control teams, DOT teams, heli-skiing tour staff, back country (bowls) tours and snow scientists.

CATEGORY III   Tour Operators Model
A.   Description – An inexpensive 1-2 meter portable probe to identify the dangerous weak layer or melt crust layer and indicate heavy density of snow on top of it; with optional temperature or other attachments.

B.   Users – Heli-skiing, skiing tours, tours for back bowls, ski area patrol personnel for quick checks, X-C alpine ski tours.

Market Survey Results

A total of twenty individuals participated in the initial Snow Probe market survey. They exemplified a fair representation from each of the three market segments and came from the US, Canada and Switzerland.

Here is a selection of the most important survey results:

Rating of importance of measurement criteria

Measurement criteria	Total points received in survey
Snow density	173
Snow water equivalent	139
Snow depth	139
Snow temperature	138
Snow grain size	127
Snow shear vs. depth	126
Snow wetness	115

Additional key survey results

	Average
How long does a daily snow survey take?	2.4 hours
How long should it take to deploy a snow probe?	10 minutes
Are you interested in transmitting recorded data?	Very interested
How deep should the snow probe go?	2.5 meters
What temperature resolution is required?	0.44°C

When asked whether a deep pit is always dug in a snow pack survey and how long does a complete survey take, the answers were different according to the market segment.
In category 1, participants tended to respond that academic-type pits are dug and these take about 2 hours.

Category 2 and 3 participants seemed more interested in analyzing specific layers so hasty pits are dug in 10 to 30 minutes.

The participants were also asked whether it would be of interest for the same snow probe to support a snow layer shear force adapter. The majority of the potential customers were enthusiastic about the idea. Its value is for monitoring weak layers and bond layer strengths and boundaries as well as timesaving over hasty pits.

Individual comments added depth to the survey. Here are some examples of the more interesting ones:

- It is important to measure the exact position of the sensor in the snowpack. For research purposed this is a must.

- The physical parameters of each snow layer are important to understanding the processes occurring in the snowpack. Pits are still required to identify and quantify weak layers. Tool as described might allow more time for these tests or for more tests increasing confidence in the results.

- The benefit for us would be speed as we could cover a lot of ground in a short period of time.

Further Product refinement

The Market Survey results were presented at the ARO International Workshop on Ice & Snow Sciences at Dartmouth College on March 7, 2001.

Two important market segments for further product development surfaced as a result of the workshop as follows:

1. Hydrology Market

The Hydrology market in the US was identified as a possible large target segment. The opportunity lies in the further development of the Show Probe to perform total water content measurements. This would be accomplished by measuring density and depth to come up with Snow Water Equivalent or Snow Water Content. These measurements are currently performed at about 600 sites in the US using a "Rose Snow Corer" in combination with "snow pillows or bladders". Time reduction could be a primary benefit of the Snow Probe.

2. Avalanche Forecasting Market

The other outcome was the definition of simplified Snow Probe model, which could be used among all of the three previously identified model categories.

It was concluded that Category 1: Scientific/Academic segment would not rely solely on a Snow Probe. They would continue to dig pits and use the snow probe as an additional reference.

One participant was quoted as saying, "Forecasters are never going to believe one method only. They will always want to have several inputs and see and feel the snow with their own hands. No one trusts one line of evidence. The Capacitec probe would be supplemental to what they do today, not a replacement."

The snow probe would appeal to all categories if it were developed into a simple portable device that shows weak layers. Another quote from the workshop "A single sensor, easy to use for dry snow only that is used to enhance the "gut feel" of avalanche forecasters. The snow probe could be used to detect how widespread a certain weak layer is."

Additional comments on pursuing a simple model were:

- Put it in a golf shaft or other very easy to deploy shaft that can be carried in a backpack and used while on skis.
- Readout should just be Vernier type, very simple with data capture using a Palm Pilot
- Take modular approach so you could add different sensor in future as an upgrade.

Figure A12 is a copy of the published specifications of the OpTek OPB706C. Because these data do not include a spatial characterization of the radiative intensity from the light-emitting photodiode, we conducted a series of optical tests on these chips.

Reflective Object Sensors
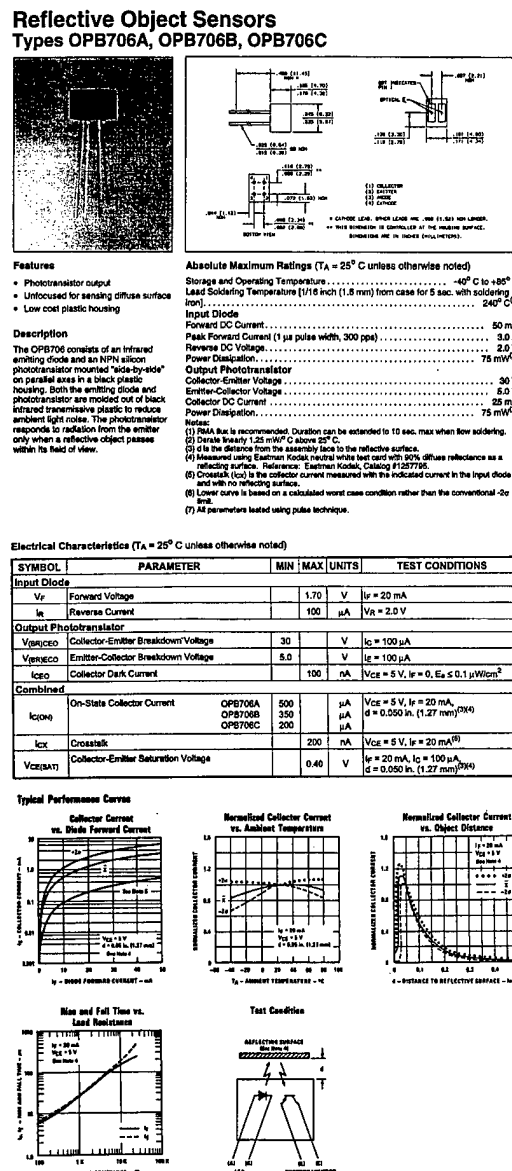**Types OPB706A, OPB706B, OPB706C**

Fig. A12. Specifications of the OpTek OPB706C.

We evaluated the optical characteristics of the OpTek OPB706C by conducting the tests sketched in Fig. A13. Two OpTek chips were located parallel to one another at three separate distances $Z = 3$ mm, 5 mm and 7 mm. In the first test, we masked the photodiode with a co-centered pinhole of diameter $D = 1$ mm and translated the latter to a distance Y on

53

the long y-axis of the photodetector. In the second test, the pinhole was co-centered on the photodetector and translated on the long axis of the photodiode. We assumed that the photodiode behaved as a modified Lambertian source producing an elementary radiative power

$$dq = I_0 \, (\cos\theta)^{n+1} \, dA \, d\omega \qquad\qquad (A15)$$

from elementary surface area dA and solid angle dω. In this expression, I_0 is a constant having units of power per unit area and unit solid angle. The value n=0 represents a Lambertian source. Values of n > 0 denote a narrower beam.
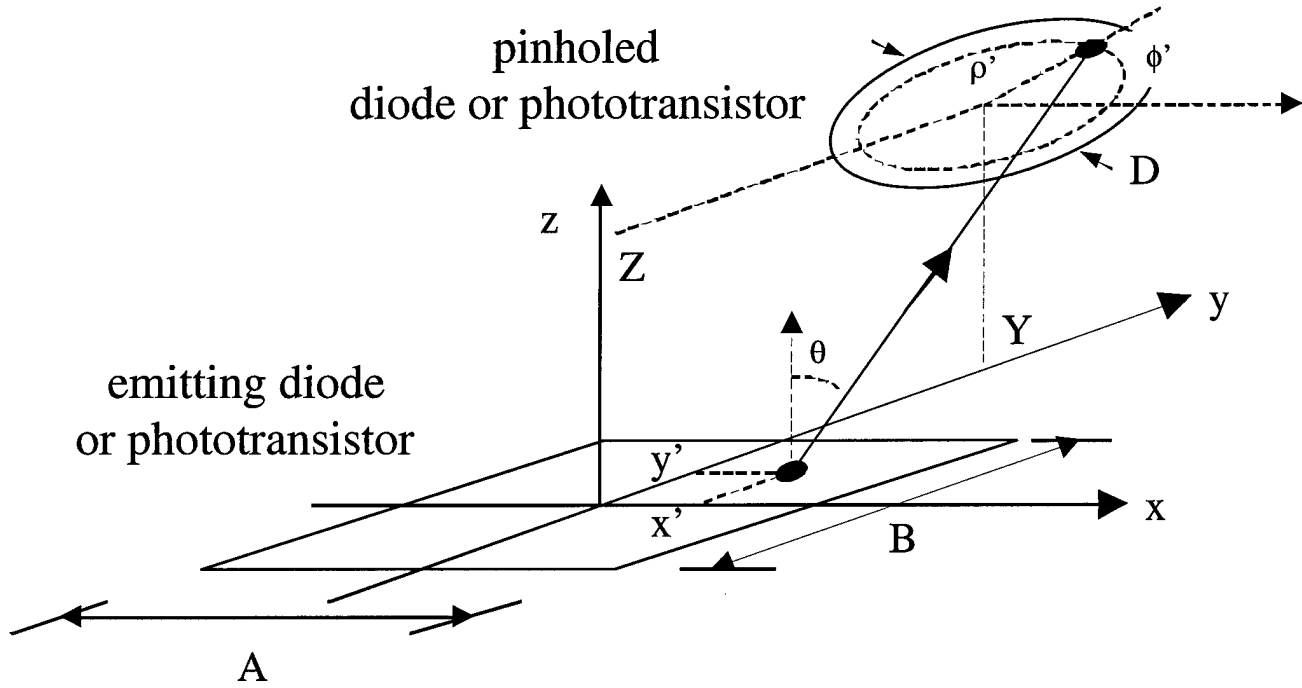

Fig. A13. Test of the photodiode and phototransistor.

We assumed that the width of the photodiode and photodetector were A = 1.3 mm. We then least-square fitted the values of B and n to the observed linear voltage signals V = V(Y,Z) recorded in the two tests. To that end, we used MatLab to integrate the radiative power numerically,

$$q = \frac{I_0}{Z^2} \int_{-A/2}^{+A/2} dx' \int_{-B/2}^{+B/2} dy' \int_0^{2\pi} d\phi' \int_0^{D/2} \rho' d\rho' \, [\cos(\theta)]^{n+4} , \qquad (A16)$$

where

$$\cos\theta = \frac{Z}{\sqrt{(x' - \rho'\cos\phi')^2 + (y' - \rho'\sin\phi' - Y)^2 + Z^2}} \, . \qquad (A17)$$

For the tests with pinholed phototransistor and with pinholed light-emitting photodiode, we found $n = 17$ (Fig. A14) and $n = 9$ (Fig. A15), respectively. We adopted the average $n = 13$ and re-computed the optimum values of $B_{detector} = 3.1$ mm for the length of the photodetector and $B_{photodiode} = 1.5$ mm for the length of the light-emitting photodiode. Figure A16 shows the corresponding narrow shape of the modified Lambertian spread in the light beam.
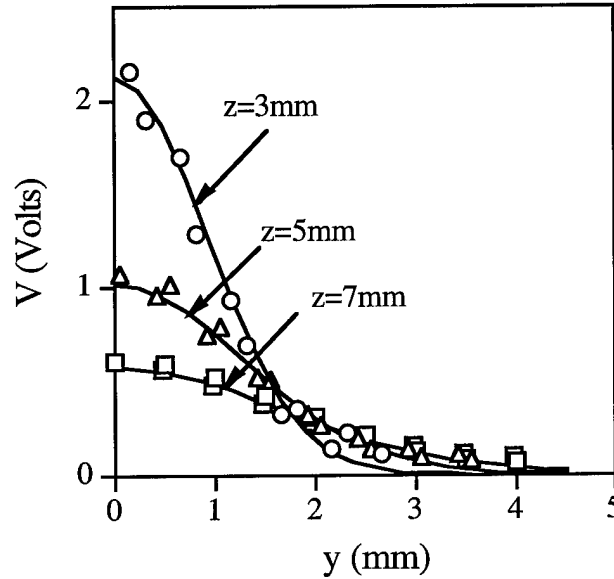
Fig. A14. Test of the light-emitting photodiode. The phototransistor is masked by a pinhole of 1 mm diameter. The circles, triangles and squares represent data obtained by translating the light-emitting photodiode along the y-direction, while the pinholed phototransistor was located at distances of z=3, 5 and 7 mm, respectively. The lines are best fits of the corresponding voltages with $n = 17$ and $B_{photodiode} = 1.7$ mm.
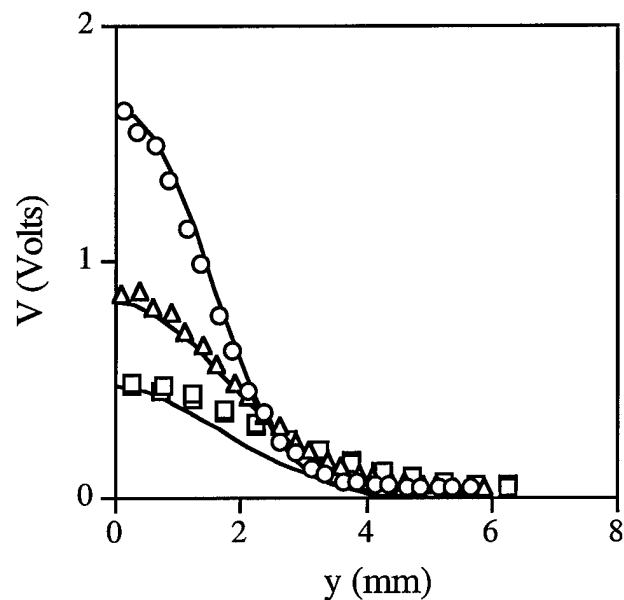
Fig. A15. Test of the phototransistor. The light-emitting photodiode is masked by a pinhole of 1 mm diameter. The circles, triangles and squares represent data obtained by translating the phototransistor along the y-direction, while the pinholed light-emitting photodiode was located at distances of z=3, 5 and 7 mm, respectively. The lines are best fits of the corresponding voltages with n = 9 and $B_{detector}$ = 3 mm.
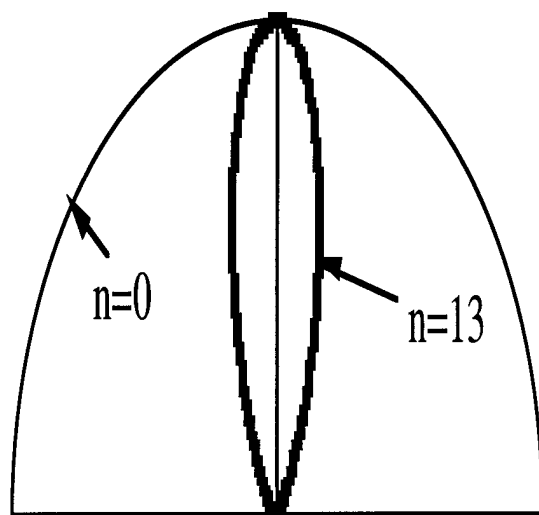

Fig. A16. Polar plot of the normalized radiation intensity $I_0 (\cos\theta)^{n+1}$ for the values of n shown. The value n=0 represents a Lambertian source; n=13 is the value we adopt for the OpTek OPB706C.

APPENDIX 6 - MONTE-CARLO SIMULATIONS

Because the 930 nm wavelength of the OpTek light-emitting photodiode is at least an order of magnitude larger than most grain diameters of interest, we chose to evaluate the backscattering properties of the snow grains adjacent to the chip using Monte-Carlo simulations based on geometrical optics, rather than considering the Mie scattering of individual snow grains. This Appendix describes the principle of these simulations.

The simulations predict the fraction of the monochromatic energy radiated by the OpTek light-emitting photodiode that returns to the phototransistor from an isotropic, homogeneous, random suspension of smooth, transparent, monodisperse, spherical, dielectric particles. Because the radiation emitted from the chip and its interaction with the particles is far more complex than a plane wave impinging on a single sphere, analytical treatment based on Mie scattering theory is impractical here. In particular, effects of diffraction (Deirmendjian, 1969; Kerker, 1969), phase shifts (Bayvel and Jones, 1981), and electromagnetic resonance (Probert-Jones, 1984) are neglected in the present analysis, as discussed below.

For spheres of diameter much greater than the wavelength of light, Deirmendjian (1969) notes that the scattered field may be estimated by tracing rays of light using classical laws of reflection and refraction at the interface, but that considering the diffraction of rays off the sphere surface would "increase the realm of applicability" of the analysis. However, for large spheres, because the diffracted light is confined within a small domain of narrow angular divergence, it is difficult to distinguish this light from the incident light (Kerker, 1969). For this reason our analysis neglects effects of diffraction.

Bayvel and Jones (1981) recommend that multiple internal reflections and phase shifts at interfaces be included in ray-tracing procedures. Accordingly, the present simulation considers all Fresnel interactions there. However, in our experiments, effects of phase shift are likely to be scrambled by the random suspension and by the complex modal structure of the diode laser that we employ. Consequently, we ignore phase shifts in this analysis.

When a plane wave impinges on a single large dielectric particle, most of the backscattered light returning directly towards the incident light is the result of a resonance of the electric and magnetic fields established within the particle (Probert-Jones, 1984). The intensity of this component exhibits large fluctuations over very small changes in the variable $\pi d/\lambda$, where d and λ are the sphere diameter and the wavelength of light, respectively. Consequently, in our experiments, the spectral distribution and the complex

modal structure of the light-emitting photodiode effectively scramble this effect. In addition, because many particles are included in the system, multiple forward scattering also returns energy to the fiber. Therefore the significance of the resonant light returning from the first sphere hit by the incident fiber emission is diminished.

Therefore, as long as the wavelength of light is much smaller than the sphere diameter, we expect that ray-tracing optics should reproduce the optical characteristics of this complex system, at least qualitatively.

The simulated suspension is made of elementary cubes of side ℓ_c containing a single sphere of diameter d. For this geometry the particle volume fraction is $(1-\varepsilon) = (\pi/6) (d/\ell_c)^3$. As a result, the largest volume fraction achievable using this simulation is that of the cubic close-pack, $\pi/6$. Cubes are arranged in rows and columns to form layers, which are laid upon each other to produce the particle matrix (Lischer and Louge, 1992). Random placement is simulated by locating the particles at random positions within the cubes and by offsetting each layer a random distance in the x- and y-directions. Unfortunately, near dense packing, because the particle structure approaches that of an offset cubic close-pack, a truly isotropic random placement is difficult to simulate using this method.

The algorithm simulates the radiation field emerging from the photodiode. The photon is emitted from a point on the face of the rectangular photodiode at a coordinate (x,y) [Fig. A13]. Its initial direction is defined by an azimuth ϕ and angle θ to the normal. The intensity I of the emitted radiation is defined as the energy flux through an elementary surface of area dA = dx dy located at (x,y) in the direction (θ,ϕ) per unit solid angle $d\omega = \sin\theta \, d\theta \, d\phi$ about this direction. Our tests of Appendix 5 indicate that the radiant intensity is approximately distributed as:

$$I = I_0 (\cos\theta)^n \tag{A18}$$

with n = 13. In this Monte Carlo scheme, the algorithm launches random photons from the optical fiber with a probability proportional to the radiant energy there. For a photon originating with x in the interval [x,x+dx], y in [y,y+dy], θ in [$\theta,\theta+d\theta$], and ϕ in [$\phi,\phi+d\phi$], that probability is

$$d^4p = \frac{I \, d\omega \, dA}{E_{tot}} = \{\frac{dx}{A}\} \{\frac{dy}{B}\} \{(n+2) \sin\theta \, (\cos\theta)^{n+1} \, d\theta\} \{\frac{d\phi}{2\pi}\}, \tag{A19}$$

where E_{tot} is the total energy emitted by the photodiode and the numerical factors are used for normalization of each term in curly brackets. From computer-generated pseudo-random numbers ξ_i with uniform probability in the interval [0,1], random variables with probabilities consistent with Eq. (A19) are obtained through the following transformations:

$$x = (\xi_1 - 0.5)\, A \tag{A20}$$

$$y = (\xi_2 - 0.5)\, B \tag{A21}$$

$$\phi = 2\pi\xi_3 \tag{A22}$$

and

$$\theta = \text{acos}[(1-r)^{1/n+2}] . \tag{A23}$$

The algorithm keeps track of each photon as it travels through the matrix. The photon may penetrate the particles through refraction, or undergo reflection inside or outside the particles. When the photon encounters a dielectric interface, the program calculates a reflection coefficient R based on the photon's angle of incidence α on the interface. Because the photon is assumed to be randomly polarized, we adopt for simplicity a value of R equal to the average of the reflection coefficients for TE and TM polarization:

$$R_{TE} = \left[\frac{n_1\cos\alpha - \sqrt{n_2^2 - n_1^2\sin^2\alpha}}{n_1\cos\alpha + \sqrt{n_2^2 - n_1^2\sin^2\alpha}}\right]^2 , \tag{A24}$$

and

$$R_{TM} = \left[\frac{n_1\sqrt{n_2^2 - n_1^2\sin^2\alpha} - n_2^2\cos\alpha}{n_1\sqrt{n_2^2 - n_1^2\sin^2\alpha} + n_2^2\cos\alpha}\right]^2 , \tag{A25}$$

where n_1 is the index of refraction of the dielectric where the incident photon is located and n_2 is that of the other dielectric. Using a random number ξ_5, the algorithm decides whether the photon is reflected ($\xi_5 \le R$) or refracted ($\xi_5 > R$) through the interface. Reflection is specular and refraction proceeds in a direction consistent with Snell's law. For the smooth particles under consideration, diffuse reflection is neglected. Note that the program keeps track of only one photon at a time. If a sufficient number of photons are launched in the simulation, this approach is equivalent to the more complicated method that would spawn two rays of light of unequal energies each time an interface is struck.

Because photon absorption through glass is negligible at this wavelength, it is ignored in the algorithm and the index of refraction of glass particles is a real number. For snow grains, the radiative power i initially equal to i_0 is absorbed along the direction x according to the Lambert-Beer's law:

$$\frac{i}{i_0} = \exp(-x/\ell_a) = \exp(-4\pi m_{im}x/\lambda) , \tag{A26}$$

59

where ℓ_a is a characteristic absorption length, m_{im} is the imaginary part of the index of refraction, and λ is the wavelength of light. For ice at $\lambda = 930$ nm, $m_{im} = 5.11 \ 10^{-7}$ and $\ell_a = 145$ mm; the real part of the index of refraction is n = 1.303 (Warren, 1984). Thus, because the size of the probe is much smaller than ℓ_a, absorption is not expected to play a major role in attenuating the infrared radiation emitted by the probe. Instead, as the simulations confirmed, most of the attenuation results from the geometrical dispersion of the scattering snow grains.

Photons leaving the matrix through the plane of the chip are either detected if they hit the active rectangle of the phototransistor, or they are lost. The fraction F_r of photons detected is an estimate of the fraction of the radiant energy that returns to the chip. Because the simulation places only a finite number of particles in front of the probe, some photons also leave through the sides or the top of the matrix. Effects of this leakage on the accuracy of the simulation are small, as Lischer and Louge (1992) demonstrated.